

Volume 4 Issue 1 December 2021 ISSN 2635-4608

Journal of Medical Imaging






VOL. 4





AIMS OF THE JOURNAL

The scope of the ScholarGen Journal of Medical Imaging (SJMI) is all about medical imaging. The SJMI publishes medical imaging theories, methods, systems and data collection, image reconstruction and image analysis. Also, SJMI covers related research fields for cell and molecular level imaging for early detection and diagnosis of disease.

SCOPE OF THE JOURNAL	JOURNAL HIGHLIGHT	Indexing
Radiography MRI Nuclear medicine Ultrasound Thermography Molecular Imaging NMR in Biomedicine Software, Tools Other studies on radiology	Radiography Magnetic Resonance Imaging Nuclear medicine Ultrasound Thermography Molecular Imaging NMR in Biomedicine Software, Tools Other studies on radiology	  

Open Access Journals by scholargen publisher is licensed under a Creative Commons Attribution-NonCommercial 4.0 International License.

4-17-27 Tenjin-cho, Kodaira, Tokyo, Japan
 Email : info@scholargen.com
 Scholargen International Cooperation

Pirogov St., 630090, Novosibirsk, Russia
 35B, Pocket B, Siddhartha Extn, New Delhi
 Private Bag X3, Rondebosch 7701, Cape Town
 75, Nowon-ro, Nowon-gu, Seoul, Korea
 Sydney, New South Wales 2052, Australia
 Valikhovsky Lane 2, Odessa, 65028, Ukraine
 Venezuela, Santa Cruz de la Sierra, Bolivia
 2329 West Mall Vancouver, BC, Canada
 Spui 21, 1012 WX Amsterdam, Netherlands

Journal of Medical Imaging

Content

ISSN 2635-4608

j. med. Imaging(ScholarGen) Volume 4, Issue 1, December 2021

1. *1H MRS Analysis Using Ultrashort-TE Sequence of Hepatic Lipids in a 9.4T MRI Device*-----
----- Jooyeon Kim
13. *Intrinsic apoptotic pathway and G2/M cell cycle arrest involved in tubeimoside I-induced EC109 cell death -*
-----Yang Xu, Guanghui Wang
17. *Determining the Degree of Malignancy on Digital Mammograms by Artificial Intelligence Deep Learning ---*
-----Sang-Bock Lee, Hwunjae Lee, V. R. Singh
33. *Evaluation of Brain Glioblastoma Images Using Podoplanin-targeted Manganese Ferrite in 9.4T MRI*-----
-----Seung-Hyun Yang, Yong-Min Huh, Hwunjae Lee
43. *LOW-DOSE LIPOSOMAL AMPHOTERICIN B IN REFRACTORY INDIAN VISCERAL LEISHMANIASIS: A MULTICENTER STUDY*----- S. SUNDAR, T. K. JHA, C. P. THAKUR, M. MISHRA, V. P. SINGH, R. BUFFELS

1H MRS Analysis Using Ultrashort-TE Sequence of Hepatic Lipids in a 9.4T MRI Device

Jooyeon Kim

Received : 25 June 2021 / Accepted : 22 November 2021 / Published online : 28 December 2021

©The Author(s) 2021

Abstract Non-alcoholic fatty liver disease is the most common cause of chronic liver diseases which is characterized by the increased level in obesity, and diabetes. Liver lipid content has been suggested to play an important pathogenic role in the development of liver fibrosis, and cirrhosis. In particular, it is associated with the risk of hepatocellular carcinoma (HCC). Liver biopsy is still the gold standard for diagnosing and assessing the disease. However, the invasive and limited tissue sampling of the biopsy presents problems. Proton magnetic resonance spectroscopy ($^1\text{H-MRS}$) enables the study of cellular biochemistry and metabolism and provides a non-invasive means to determine disease abnormalities and progression in vivo and longitudinally. With the increased availability of high-field magnetic resonance (MR) systems for clinical and preclinical studies, both signal-to-noise ratio (SNR) and spectral resolution of metabolites in the MR spectra can be improved significantly, allowing more accurate metabolite identification, quantification and thus disease characterization. $^1\text{H-MRS}$ permits longitudinal assessment of fat fraction, saturated and unsaturated. This study is to characterize early hepatic lipid changes in fatty liver mouse model by in vivo short-echo time (TE) $^1\text{H-MRS}$ (Proton-Magnetic Resonance Spectroscopy).

This study examined 17 male C57BL/6 mice, including 8 high-fat diet (45%) mice for 20 weeks and 9 normal mice for 17 weeks. C57BL/6 mice were fed with 60% high fat diet containing 60% fat, 20% protein and 20% carbohydrate. MR imaging with single-voxel $^1\text{H-MRS}$ was performed using a PRESS sequence at 9.4T magnetic resonance imaging (MRI). The full width at half maximum (FWHM) ranged from 4 to 8 Hz. Water suppression was accomplished with "VAPOR" pulses. The examination (voxel size, $2 \times 2 \times 2 \text{ mm}^3$) were performed from liver parenchyma in mice at normal and at high-fat diet, respectively. The spectral acquisition parameters were TR/TE = 2500/16 ms, and 256 acquisitions for averaging. LCModel fitting was conducted using experimental basis sets. Less than 10% standard deviation (%SD) of metabolite quantification data was allowed. The areas under the peaks were measured as the follows: signal integrals of lipid methyl protons ($-\text{CH}_3$; 0.9 ppm), methylene proton ($(-\text{CH}_2)_n$; 1.3 ppm), allylic protons ($-\text{CH}_2-\text{C}=\text{C}-\text{CH}_2$; 2.1 ppm), α -methylene protons ($-\text{CO}-\text{CH}_2-\text{CH}_2$; 2.3 ppm), diallylic protons ($=\text{CCH}_2-\text{C}=\text{C}$; 2.8 ppm), glycerol protons (CH_2-COO ; 4.1 ppm), glycerol protons (CH_2-COO ; 4.3 ppm) and methene protons ($\text{CH}=\text{CH}$; 5.3 ppm). For relative quantification, total lipid (TL), total saturated fatty acid (TSFA), total unsaturated fatty acid (TUFA), total unsaturated bond (TUB), polyunsaturated bond (PB) and choline-containing compound (Cho) were normalized by separating each peak of $(-\text{CH}_2)_n$, $-\text{CH}_2-\text{C}=\text{C}-\text{CH}_2$, $-\text{CO}-\text{CH}_2-\text{CH}_2-\text{C}-\text{CH}_2-\text{C}=\text{C}$ and $-\text{CH}=\text{CH}$.

¹Jooyeon Kim 

Department of Research Equipment Operation
Korea Basic Science Institute, Cheong-won, Ochang,
Republic of Korea

Significant increases in lipid signals of 0.9, 1.3, 2.1, 2.3, 2.8, 4.1, 4.3, and 5.3 ppm were found in animals at high-fat diet ($p < 0.01$, $p < 0.001$). TL, TSFA, TUFA, TUB, PUB and Cho were significantly increased at high-fat diet ($p < 0.01$, $p < 0.05$). Therefore, $^1\text{H-MRS}$ is useful in detecting and characterizing various hepatic lipid alterations.

Key word : Fat liver; Hepatic lipids; MRS; Ultrashort TE; 9.4T MRI

1. INTRODUCTION

Obesity increases death rate by causing liver disease, diabetes, gallstones, chronic hepatitis, cerebrovascular disorders, and heart disease^[1]. There is NAFLD (non-alcoholic fatty liver disease) in liver disease that causes obesity. NAFLD is a disease in which triglycerides are accumulated in hepatocytes regardless of alcohol consumption. Currently, 30% of the total population falls under NAFLD, and 90% of patients who underwent surgery for severe obesity are considered to be due to NAFLD^[2]. NAFLD is associated with obesity and diabetes, and liver lipid content has been known to play an important role in the development of liver fibrosis and cirrhosis^[3]. Animal model experiments for hepatocellular carcinoma are starting, but additional studies are needed for treatment, diagnosis, and prevention^[4].

$^1\text{H-MRS}$ can provide the chemical structure or state of metabolites in vivo in a non-invasive method^[5], and has been used to diagnose non-alcoholic fatty liver disease^[6]. Recently, the development of high magnetic field devices has greatly improved the signal-to-noise ratio (SNR) and resolution of magnetic resonance imaging system.

Therefore, it is necessary to identify and quantify metabolites in vivo using a high magnetic field magnetic resonance system to determine the characteristics of NAFLD^[7]. The high magnetic field magnetic resonance imaging system can analyze the

signals of lipid metabolites such as total lipid, total saturated fatty acid, total unsaturated fatty acid, total unsaturated bond, and polyunsaturated bond using $^1\text{H-MRS}$. Choline-containing compounds can be analyzed using $^1\text{H-MRS}$ through signal integration of Lipid methyl protons ($-\text{CH}_3$; 0.9 ppm), Methylene protons ($(-\text{CH}_2)_n$; 1.3 ppm), Allylic protons ($-\text{CH}_2-\text{C}=\text{C}-\text{CH}_2$; 2.1 ppm), α -methylene protons ($-\text{CO}-\text{CH}_2-\text{CH}_2$; 2.3 ppm), Diallylic protons ($=\text{C}-\text{CH}_2-\text{C}=\text{C}$; 2.8 ppm), and methene protons ($-\text{CH}=\text{CH}-$; 5.3 ppm) (Cheung et al. 2011).

The purpose of this study was to analyze liver lipid metabolites and fatty acid components of normal mouse and fatty liver mouse through $^1\text{H-MRS}$ using ultra-high magnetic field 9.4T MRI. We are trying to characterize non-alcoholic fatty liver disease through analysis.

2. EXPERIMENTAL METHODS

2.1. Experimental animals

The experiment was conducted for 20 weeks. In the laboratory environment, the temperature was set to 22 degrees Celsius, and the humidity was set to 50% to 60% and checked every 12 hours. A total of 17 animals were divided into 8 control animals and 9 experimental groups. The control group was fed a general diet containing mainly carbohydrates and proteins, and the experimental group was fed a high-fat diet containing 60% carbohydrates, 20% fat, and 20% protein. The weight and blood glucose levels of the control and experimental mice were measured for each week of age. Breathing was monitored, and warm water was circulated through the heating pad to maintain body temperature at 36.5 degrees.

Pulse sequence for MRI used a PRESS (point-resolved spectroscopy) sequence. After the MRI experiment, for histopathological evaluation, liver tissue was excised and the liver samples were fixed

in formalin. The sufficiently fixed tissue was washed with water to remove an excessive amount of fixing reagent. In order to embedding by infiltrating paraffin that does not mix with water into the liver tissue, the liver tissue was dehydrated using alcohol with a difference in concentration. Dehydration was gradually processed from a low-concentration alcohol solution to a high-concentration alcohol solution, followed by treatment with pure 100% alcohol and benzene. Paraffin dissolved in benzene as an organic solvent was penetrated into the dehydrated tissue, and then treated with pure paraffin in the liquid state at high temperature (60°C) to completely penetrate. The paraffin that has penetrated into the tissue was cooled at low temperature to make a solid-state, and then cut into appropriate size and trimmed. It was cut to an appropriate thickness(3~20 μm) in a thin-cutting machine. The sliced tissue adhered to a glass slide, and tissue paraffin was removed with xylene, an organic solvent. Since most staining solutions are aqueous solutions, the slides with liver tissues were hydrated by treating them with a high concentration of alcohol to a low concentration of alcohol aqueous solution. Primary staining was performed with an aqueous hematoxylin solution. At first, after staining it thick, it was stained through the process of properly matching the staining degree of the sample that was excessively stained with an alcohol solution. Then, secondary staining was performed with eosin. Hematoxylin was stained blue when it encountered acids such as the nucleus of cells and other acidic structures (the cytoplasm is rich in RNA, cartilage matrix). And eosin met basicity and stained other cytoplasmic components and collagen in red. After the first and second staining was done, a microscopic examination was performed. The stained results were read by two pathologists. The level was decided by comparing the liver of the control group and the liver of the experimental group with the level of the

pathology score. As a result of the comparison, the degree of fat content and the degree of inflammation were discriminated from 0 to 3.

2.2. 9.4T MRI

A number of studies have been performed on the imaging of mice using 9.4T MRI equipment^[8]. The purpose of this study is to find a method for diagnosing non-alcoholic fatty liver similar to an invasive histopathological examination by confirming that the signals of lipid metabolites are clearly different in 9.4T MRI for animals. This is because the recent introduction of the high magnetic field (≥ 3.0 Tesla) MRI devices is expanding, and high magnetic field MRI devices provide high SNR and spectrum resolution so that the peaks for each material are well separated in MRS. The 4-channel animal coil used in this experiment is a 9.4T-only coil, and it is able to greatly improve SNR and resolution by putting it closer to the experimental mouse. Figure 1(a) is a 9.4 Tesla (Broker System 9.4T animal MRI device) and Figure 1(b) is a picture of a 4-channel mouse heart receive-only animal coil.

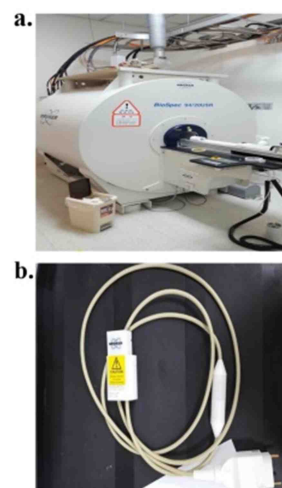


Figure 1. Broker system 9.4T animal MRI(a) and a 4-channel mouse heart receive-only array animal coil(b)

2.3. MR signal acquisition

In 9.4 T MRI, T2-weighted fast spin-echo was used to obtain the transverse, sagittal, and coronal (FOV 60 mm × 60 mm, slice thickness = 1.5 mm) in the axial direction of three sections. 1H-MRS used a Point-resolved spectroscopy (PRESS) sequence^[9]. In order to determine the 3D position of the ROI with the PRESS sequence, a 90° slice selective RF pulse and a 180° RF pulse are applied twice^[10]. During the 90° pulse stimulation, the z-direction slice is determined by the gradient magnetic field G_Z. During the following two 180° pulse stimuli, G_y and G_x determine the thickness of the slices in the y and x directions, similar to the principle of determining the z-direction slice, and the volume of interest is determined as the intersection point of the three slices found.

As a parameter, TR/TE = 2500/16 ms was used, and data were obtained with a matrix size of 256. The single voxel method was used, and the voxel size was 2×2×2 mm³ so that the largest blood vessels were avoided and placed in the uniform liver parenchyma. In particular, the 1H-MRS voxel size can create a smaller voxel size as the magnetic field strength of the magnet increases, and in general, the optimal voxel amount is determined through the signal-to-noise ratio and scan time.

Typical water peak signals were suppressed using variable power and optimized relaxation delays (VAPOR) pulses, and the line width (FWHM) included 37-69 Hz (mean±SD, 52.1±9.62 Hz). For each lipid metabolite, the baseline was 0 weeks before feeding the high-fat diet, and the concentration values of the metabolites were measured and the percent (%) was calculated by comparing by week age.

Lipid metabolites below the peak are listed in Table 1,

Lipid methyl protons (-CH₃; 0.9 ppm), Methylene protons ((-CH₂-)_n; 1.3 ppm), and Allylic protons (-CH₂-C=C-CH₂; 2.1 ppm).), α-methylene protons (-CO-CH₂-CH₂; 2.3 ppm), Diallylic protons (=C-CH-2-C=; 2.8 ppm), glycerol protons (CH₂-COO; 4.1 ppm), glycerol protons (CH₂ -COO; 4.3 ppm) and methene protons (-CH=CH-; 5.3 ppm) were measured^[11]. Fatty acid components of each of these lipid metabolites were calculated using a mathematical formula, and the percentage (%) was obtained by measuring the concentration of the metabolite by comparing each week with age 0 weeks before feeding the high-fat diet.

Fatty acid components in Table 2 are total lipid, total saturated fatty acid, total unsaturated fatty acid, total unsaturated bond, polyunsaturated bond, It was measured as choline (Choline-containing compound, CCC)^[12]. Considering the fact that the SNR is similar between spectra due to the same voxel size and hardware configuration for total lipid and choline, (-CH₂-)_n, CCC was quantified by dividing the peak by spectral noise. In addition, total saturated fatty acid, total unsaturated fatty acid, total unsaturated mixture, polyunsaturated mixture were peaked by (-CH₂-)_n, -CH₂-C=C-CH₂, -CH=CH-, =C-CH-2-C by -CH₃ Was quantified by dividing^[13].

Table 1. Peak area ratio of various metabolite name in proton magnetic name in proton magnetic resonance spectroscopy(¹H-MRS)

No	Name	Peak area ratio	Chemical shift
1	methyl	-CH ₃	0.9 ppm
2	methylene	-(CH ₂) _n -	1.3 ppm
3	allylic	-CH ₂ -CH=CH-CH ₂ -	2.1 ppm
4	α-methylene	-CO-CH ₂ -CH ₂	2.3 ppm
5	diallylic	-CH=CH-CH ₂ -CH=CH-	2.8 ppm
6	glycerol	CH ₂ -COO	4.1 ppm
7	glycerol	CH ₂ -COO	4.3 ppm
8	vinyl	-CH=CH-	5.3 ppm

Table 2. Fatty acid ratios and resonant frequency(ppm) in proton magnetic resonance spectroscopy(¹H-MRS)

Index of fatty acid	Fatty acid component
Total lipid	Lip13
Total saturated fatty acid	3×Lip13/2×Lip09
Total unsaturated fatty acid	3×Lip20/4×Lip09
Total unsaturated bond	3×Lip53/2×Lip09
Polyunsaturated bond	3×Lip28/2×Lip09
Choline-containing compound (CCC)	Lip32

2.4 Statistical analysis

Raw data obtained through 1H-MRS were analyzed using LCMoel software (Linear Combination of Model, Version 6.3-1H, Stephen W. Provencher). LCMoel is a widely used algorithm, and it is a method of quantifying magnetic resonance spectroscopy using a semi-parametric NLLS(Non Linear Least Square) method based on a priori information through metabolite base set. The model is built on the basis of the real part of the Fourier transformed spectrum and consists of two parts. The first is the term that describes the baseline, and the second is the term that describes the spectral line shape.

The model is as follows.

$$\hat{Y}[\nu_k] = e^{-i(\alpha_k + \nu_k \tau)} \left[\sum_{j=1}^{N_B} \beta_j B_j(\nu_k) + \sum_{i=1}^{N_M} c_i \sum_{n=-N_S}^{N_S} S_n M_i(\nu_k - n; \gamma_i, \epsilon_i) \right]$$

$$Y[\nu_k] = \hat{Y}[\nu_k] + \epsilon[\nu_k] \text{ ----- (1)}$$

What we want to find in the end using the model is to find P, B, and S that satisfy the conditions that minimize the equation below.

$$\frac{1}{\sigma^2(Y)} \sum_{k=1}^N (R[Y(\nu_k) - \hat{Y}(\nu_k)])^2 + \| \alpha_{\mathcal{P}} R_{\mathcal{P}} \|^2 + \| \alpha_{\mathcal{B}} R_{\mathcal{B}} \|^2 + \sum_{i=1}^M \left(\frac{|\gamma_i - \beta|^2}{\sigma^2(Y)} + \frac{\epsilon_i^2}{\sigma^2(\epsilon_i)} \right)$$

$$\text{Constraint : } \gamma_1 \geq 0, \epsilon_j \geq 0, \sum S = 1 \text{ ----- (2)}$$

This minimization process is performed using CONTIN, a uniform nonlinear least-squares method developed by Dr. Provencher^[14]. The baseline of the spectrum is modeled by LCMoel using the cubic B-spline method. In addition, the metabolite database obtained by in vitro measurement or simulation is stored internally in the LCMoel^[15]. The error estimation is given through the CRLB(Cramer-Rao lower bound), where CRLB is the theoretical minimum of the variance (σ²) that an estimator (e.g., metabolite concentration) can take. And is defined as the inverse of Fisher's information F as follows.

$$\sigma^2 \geq F^{-1} = CRLE$$

$$F = E \left[\left(\frac{\partial \ln L}{\partial p} \right)^T \left(\frac{\partial \ln L}{\partial p} \right) \right] \text{ ----- (3)}$$

Here, L represents a likelihood function, p=(P1,P2,...,PN) represents a model parameter, T represents a transpose, and E represents an expectation value. In general, a likelihood function is assumed to determine what distribution the rest, which is the difference between the measured data and the model function, will be shown. In the case of LCMoel, it has not yet been reported how to accurately calculate CRLB^[16]. This algorithm requires a base set, a collection of pure metabolite spectra, in order to quantify the concentration of metabolites present in the acquired signal. The metabolite signals that make up the base set are fitted to the acquired spectrum, which includes a spline function to model the lower part of the spectrum baseline due to a sufficiently uninhibited water signal or macromolecules. For linear combination model fitting, an experimental basis set (LCMoel provided) was used. For the basis set, curve fitting was performed using the basis set

provided by LCModel. A standard deviation (%SD) of less than 10% of the lipid metabolite quantification data was allowed. Error estimation was used as a useful reliability indicator through the CRLB named %SD. In order to see the difference in fatty acids quantified in the liver of normal mouse and in the liver of mouse induced by a high fat diet, SPSS version 21 software package (SPSS, Chicago, IL, USA) was used to analyze. For each interlipid metabolite and fatty acid component, it was expressed as mean \pm standard deviation. Paired student's t-test was performed. At this time, a value of $p < 0.05$ was judged to have statistical significance.

3. RESULT

For the experiment, 6-week-old male mice (C57BL/6 mice) weighting 20 ± 5 gram were fed a general diet to 8 control animals, and 9 mice in the experimental group were fed a high fat diet (fat-60%, protein-20%, Carbohydrates -20%) were fed. Thereafter, at 20 weeks, the parenchymal tissues of 9 mice in the experimental group were examined.

3.1. Fatty liver mouse model weight and blood glucose level comparison by week

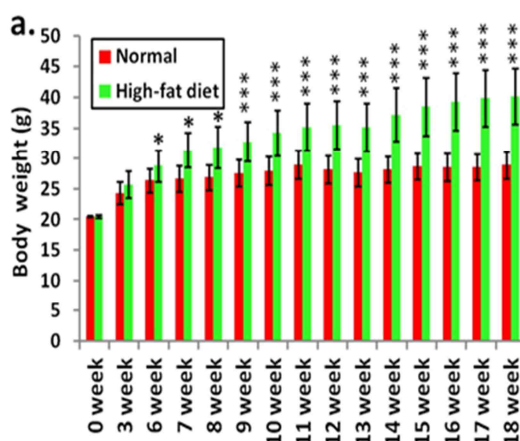
Figure 2(a) shows the results of measuring the weight of the control group and the experimental group for each week. After 6 weeks, the control group was 26.4 ± 3.24 g and the experimental group was 28.8 ± 2.20 g. These results indicate statistical significance ($p < 0.05$) (Table 3). In addition, Figure 2(b) shows the blood glucose measurement results after 11 weeks. As a result of measuring blood glucose, the control group was 98.7 ± 2.34 g and the experimental group was 136 ± 3.20 g. This result also showed a statistically significant increase ($p < 0.01$) (Table 4).

Table 3. Body weight(g) indices in proton magnetic resonance spectroscopy ($^1\text{H-MRS}$) at 9.4T MRI

Week	Normal	High-fat diet	P-value
0	20.5	20.5	0.000
3	24.4	25.7	0.116
6	26.4	28.8	0.019
7	26.7	31.4	0.001
8	26.9	31.9	0.001
9	27.6	32.8	0.000
10	28	34.2	0.000
11	29	35.2	0.002
12	28.2	35.5	0.000
13	27.7	35.1	0.000
14	28.2	37.2	0.000
15	28.7	38.5	0.000
16	28.6	39.3	0.000
17	28.6	39.9	0.000
18	28.9	40.2	0.000

Table 4 Blood sugar indices in proton MRS at 9.4 T MRI

Week	Normal	High-fat diet	P-value
8	102.6	110.8	0.210
11	97.6	127.6	0.002
13	147.6	169.3	0.001
16	139.3	170.8	0.008
17	138	170.8	0.009



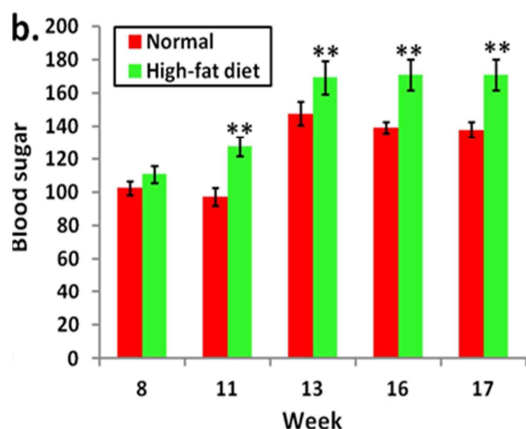


Figure 2. Body weight(g)(a) and blood sugar(b) in normal mice compared to high fat mice. Data shows mean±SD for each group using a two tailed *t*-test with significance threshold of **p*<0.05, ***p*<0.01, ****p*<0.001.

3.2. Comparison of liver lipid metabolites in vivo

Through 1H-MRS, the metabolites of interlipid metabolites corresponding to 0.9, 1.3, 2.1, 2.3, 2.8, 4.1, 4.3 and 5.3 ppm are shown. Through this, it can be seen that the corresponding interlipid metabolites appear differently for each frequency. Interlipid metabolites corresponding to 4.1 and 4.3 ppm, which were not seen in previous 3T MRI, were found. Lipid metabolites below the peak were measured as shown in Table 7. Figure 3 shows the comparison of the liver lipid metabolites of the control group and the liver lipid metabolites of the experimental group in 1H-MRS, and there was a statistically significant difference with an increase of 0.9 ppm (*p*<0.01). In addition, there was a statistically significant difference as 1.3, 2.3, 2.8, 4.1, 4.3 and 5.3 ppm increased (*p*<0.001) (Table 5).

Table 5. Lipid signals indices in proton magnetic resonance spectroscopy(¹H-MRS) at 9.4T MRI

Name	Normal	High-fat diet	<i>P</i> -value
Lip09	0.010	0.080	0.007
Lip13	0.066	0.466	0.000
Lip21	0.012	0.078	0.000
Lip23	0.006	0.060	0.000
Lip28	0.005	0.032	0.000
Lip41	0.005	0.023	0.000
Lip43	0.005	0.023	0.000
Lip53	0.011	0.106	0.000

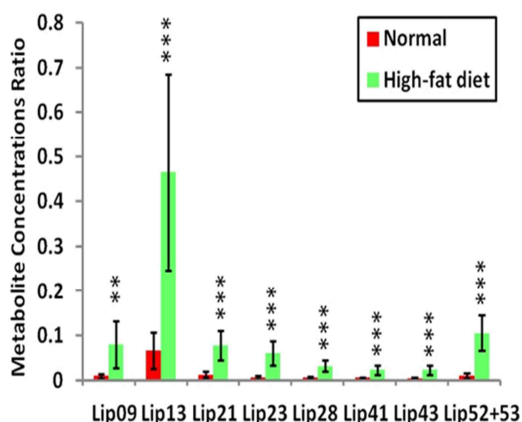


Figure 3. Lipid signals quantified normal and 20 weeks after high fat diet. Data shows mean±SD for each group using a two tailed *t*-test with significance threshold of ***p*<0.01, ****p*<0.001.

3.3. Comparison of liver fatty acid components in vivo

Figure 4 shows the lipid metabolites obtained using a mathematical formula. The percentage (%) was calculated by comparing the liver fatty acid component of the control group and the liver fatty acid component of the experimental group. When comparing the liver fatty acid components of the control group and the liver fatty acid components of the experimental group, there was a statistically

significant difference due to an increase in total lipids ($p < 0.01$). Also, there was a statistically significant difference due to the increase in saturated fatty acid, unsaturated fatty acid, unsaturated mixture, polyunsaturated mixture, and choline ($p < 0.05$) (Table 6).

Table 6. Fat fraction indices in proton magnetic resonance spectroscopy ($^1\text{H-MRS}$) at 9.4T MRI

Name	Normal	High-fat	P-value
TL	0.066	0.466	0.001
TSFA	0.012	0.068	0.020
TUFA	0.010	0.054	0.038
TUB	0.018	0.087	0.011
PB	0.010	0.045	0.040
CCC	0.019	0.057	0.034
UI	0.108	0.155	0.030

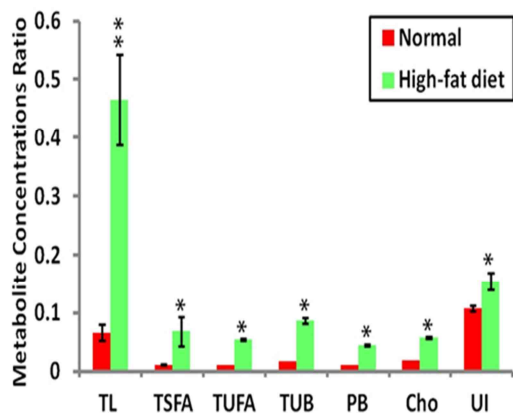


Figure 4. Fat fractions quantified normal and 20 weeks after high fat diet. Data shows mean \pm SD for each group using a two tailed t -test with significance threshold of $*p < 0.05$, $**p < 0.01$.

3.4. Histopathological evaluation

Figure 16(a) shows the comparison of hepatocytes of the control group and the hepatocytes of the experimental group. It was found that fat accumulation was significantly increased in the

hepatocytes of the experimental group, and conventional cell necrosis and apoptosis were observed. Iron pigmentation is indicated in bright blue, nuclei in red, and cytoplasm in bright pink. Figure 16(b) shows that two pathologists compared the control liver cells and the experimental group liver cells with the mean pathology score level. As a result of comparison, the score of inflammation increased, but there was no statistically significant difference. On the other hand, the score of steatosis increased and was statistically significantly higher ($p < 0.05$, $p < 0.001$) (Table 13).

Table 7. Pathological score reading's indices of normal and high-fat diet liver in Hematoxylin-eosin (H&E) staining at Microscope

Reader	Name	Normal	High-fat	P-value
Reading 1	Inflammation	0.111	0.375	0.389
	Steatosis	0.222	2.250	0.000
Reading 2	Inflammation	0.111	0.375	0.378
	Steatosis	0.444	1.625	0.048

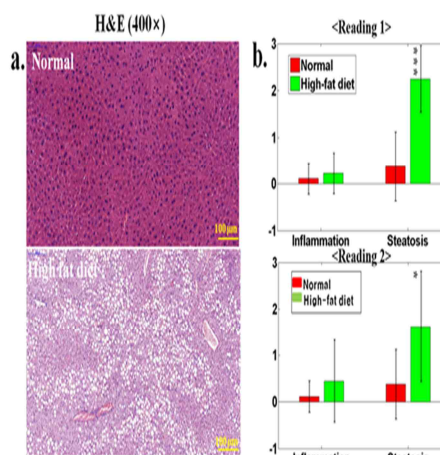


Figure 5. Typical hematoxylin-eosin(H&E) staining(400 \times ; left column) normal liver(a, top) and livers subjected to high-fat diet liver(a,bottom) and pathological scores for 20 weeks(b). Data shows mean \pm SD for each group using a two tailed t -test

with significance threshold of * $p < 0.05$, *** $p < 0.001$.

4. Discussion

In this study, it was demonstrated that 1H-MRS can be used to detect interlipid abnormalities in fatty liver disease. The 1H-MRS is the most standard MR image scanner for obtaining high-resolution images and functional information. It has been used to investigate local liver lesions and has been found to be useful by characterizing human and animal liver cancer models.

4.1. Difference between 1H-MRS PRESS and STEAM

Unlike ultrasonography, which subjectively determines the presence of fatty liver, 1H-MRS can non-invasively measure the visceral fat area and the degree of liver fat infiltration by objective values. Therefore, it is possible to diagnose fatty liver by accurately and quantitatively measuring it, and it is useful for follow-up observation of improvement in health status after diagnosis^[17]. In this study, the highest magnetic field was used to study fatty liver compared to previous studies. At high magnetic fields, 1H-MRS provides a high-quality spectrum within an acceptable scan time due to the inclusion of a good SNR and increased spectral resolution. This study confirmed in vivo accurate biochemical information that can be used for characterization and monitoring of liver diseases including fatty liver in 9.4T MRI. In previous studies, it was relatively difficult to accurately analyze and quantify multiple lipid signals due to limited spectral resolution. On the other hand, in this study using 9.4T MRI, various lipid peaks (eg, $-\text{CH}_2-\text{C}=\text{C}-\text{CH}_2-$, $=\text{C}-\text{CH}_2-\text{C}=\text{C}-$, $-\text{CH}=\text{CH}-$) were analyzed in the fatty liver. Through

this, accurate information on the lipid composition was obtained. Currently, 1H-MRS is divided into two methods: a single voxel technique and a multi-voxel technique. The single-voxel technique is a single volume method that selects one 3D pixel at a local area in an MR image, and because this method can be obtained with a high-frequency resolution, it is easy to distinguish each metabolite and the data analysis time is short. The multi-voxel technique is a multi-volume method for obtaining multiple 3D pixels by adding an additional selective gradient. In this method, a CSI(chemical shift imaging) image is also possible to image information of specific metabolites from each location. STEAM(stimulated echo acquisition method) is a method of continuously giving three-time slice-selective 90° RF pulses. If three RF waves were selected on a right-angled plane, a stimulated echo would be obtained only in the volume of the three samples at the intersection of the right-angled planes. Generally, the CHESS pulse is used to suppress the water signal, and the size of the signal appears smaller than PRESS. In PRESS(point resolved spectroscopy), a 90° slice selective RF pulse is applied and then 180° RF pulses are applied twice. PRESS sequence is the same as the STEAM sequence and includes CHESS pulse waveform. If a 180° pulse is used and the SNR is approximately two times higher than that of stimulated echo by spin echo, it can be used in a local area of about 1 cc ($1 \times 1 \times 1 \text{ cm}^3$). In the abdominal magnetic resonance spectroscopy test, because the SNR is low due to respiration, the PRESS method, which has an SNR of about 40% or more compared to the STEAM method, had superior results in this experiment.

4.2. Efficacy of high magnetic field 9.4T MRI

The characteristics of this study using high magnetic field 9.4T MRI are as follows.

- (1) High magnetic field 1H-MRS can obtain information on various lipid metabolites by separating two peaks of lipid metabolites well. Through 9.4T MRI, the 4.1 and 4.3 peaks were well separated and information on various lipid metabolites could be obtained due to the high magnetic field's 1H-MRS resolution^[18].
- (2) Respiration was continuously monitored to reduce artifacts caused by respiration, and uniform hepatic parenchymal tissue was obtained using a long TR.
- (3) In order to correct the non-uniform magnetic field to a uniform magnetic field, the noise was blocked in the region of interest by repeatedly shimming.
- (4) The accuracy of quantification of fatty acid components was improved by examining pathological tissue specimens^[19].

4.3. Comparison of liver lipid metabolites and fatty acid components in vivo

When comparing lipids and saturated fatty acids 2 weeks after starting the high-fat diet, the concentration of metabolites was significantly increased ($p < 0.01$). The most significant changes in lipid and saturated fatty acid showed that the increase of saturated fatty acid was mainly involved in the increase of lipid. It was found that the increase in lipid was due to fat infiltration and changes in hepatocytes. It was found that the increase of saturated fatty acid in the liver is related to activated cell death induced by saturated fatty acid^[20]. In non-alcoholic fatty liver disease, endoplasmic reticulum stress associated with increased saturated fatty acids in the liver has been shown to promote liver damage. It partially contributed to the progression of diseases ranging from simple fatty liver to fatty hepatitis. In unsaturated fatty acids, unsaturated mixtures, and polyunsaturated mixtures, a significant increase in metabolite concentration was observed ($p < 0.05$).

More unsaturated double bonds were formed and increased in monounsaturated fatty acids 2 weeks after eating a high-fat diet^[21]. This increased degree of polysaturation and increased cell necrosis and death were observed in various experimental models. After hematoxyline-eosin staining for histological evaluation, hepatic fat accumulation was confirmed^[21]. In 2014, Pacifico and Scorletti, a study found that administration of n-3 PUFA affected non-alcoholic fatty liver. Therefore, the long-term administration of a high-fat diet may indirectly be a factor that may adversely affect the liver.

4.4. Limitation of this study and future studies

The limitations of this study are as follows. In 9.4T MRI, the age and number of mice in the control group and the experimental group are different. The experiment was attempted to be divided by week age as much as possible, but due to movement artifacts caused by breathing during the experiment, breathing monitoring had to be continuously performed, and it took a long time to perform one test, so the age of the week was different. There was a case where the experimental mice died during the experiment, and the number of the control group and the experimental group became insufficient. Therefore, in future studies, it is necessary to diversify the types of control and experimental groups, increase the number of experimental mice, and conduct experiments under the same conditions. If so, it is thought that it will be able to provide a new direction for accurate quantitative evaluation of liver disease models.

5. Conclusion

In this study, a hepatic steatosis model was established by verifying that the lipid signal in the liver parenchyma of mice increased for a long time

20 weeks after feeding a high-fat diet through ¹H-MRS in a 9.4T MRI experiment. As a result of the evaluation by the histopathological method, it was not possible to confirm even a liver fibrosis model. In the future, by injecting a CCl₄ solution into olive oil, various chemical substances secreted from kupffer cells, which are macrophages in the liver, change the phenotype of hepatocytes and astrocytes, thereby will test the mechanism of accumulation of extracellular matrix such as collagen. Based on this, we will establish a liver fibrosis model by magnetic resonance spectroscopy. In addition, the high magnetic field ¹H-MRS and MRI will be useful for diagnosing fatty liver by accurately measuring the visceral fat area and liver fat infiltration degree non-invasively, and for follow-up observation of improvement in health status after diagnosis. If such research is carried out continuously, it will be possible to develop new therapeutic drugs and propose new treatment methods by analyzing changes in a wide range of metabolites through quantitative evaluation of liver disease models.

[Reference]

- [1] Fabbrini, E., Sullivan, S. and Samuel, K. (2010). "Obesity and nonalcoholic fatty liver disease: biochemical, metabolic, and clinical implications," *Hepatology*, 51(2), 679-689.
- [2] Angulo, P.(2002), "Nonalcoholic fatty liver disease," *New England Journal of Medicine*, 346(16), 1221-1231.
- [3] Ekstedt, M., Franzen, L. E., Mathiesen, U. L., Mathiesen, L., Thorelius, L., Holmqvist, M. and Bondemar, G.(2006). "Long-term follow-up of patients with NAFLD and elevated liver enzymes," *Hepatology*, 44(4), 865-873.
- [4] Bataller, R. and Brenner, D. A.(2005), "Liver fibrosis," *The Journal of clinical investigation*, 115(2), 209-218.
- [5] Zhong, K. and Emst, T.(2004), "Localized in vivo human ¹H MRS at very short echo times," *Magnetic Resonance in Medicine: An Official Journal of the International Society for Magnetic Resonance in Medicine*, 52(4), 898-901.
- [6] Marsman, H. A., Van Werven, J. R., Nederveen, A. J., Ten Kate, F. J. Heger, M., Stoker, J. and Van Gulik, T. M.(2010), "Noninvasive Quantification of Hepatic Steatosis in Rats Using 3.0 T ¹H-Magnetic Resonance Spectroscopy," *Journal of Magnetic Resonance Imaging*, 32(1), 148-154.
- [7] Hamilton, G., Middleton, M. S., Bydder, M., Yokoo, T., Schwimmer, J. B., Kono, Y., Patton, H. M., Lavine, J. E. and Sirlin, C. B.(2009), "Effect of PRESS and STEAM sequences on magnetic resonance spectroscopic liver fat quantification," *Journal of Magnetic Resonance Imaging: An Official Journal of the International Society for Magnetic Resonance in Medicine*, 30(1), 145-152.
- [8] Lee, Y. J., Jee, H. J., Noh, H. J., Kang, G. H., Park, J. Y., Cho, J. G., Cho, J. H., Ahn, S. D., Lee, C. H., Kim, O. H., Oh, B. C. and Kim, H. J.(2013), "In Vivo ¹H-MRS Hepatic Lipid Profiling in Nonalcoholic Fatty Liver Disease: An Animal Study at 9.4T," *Magnetic resonance in medicine*, 70(3), 620-629.
- [9] Bazelaire, D., Cedric, M. J., Duhamel, G. D., Rofsky, N. M. and Alsop. D. C.(2004), "MR imaging relaxation times of abdominal and pelvic tissues measured in vivo at 3.0 T," *Hepatology*, 230(3), 652-659.
- [10] Bottomley. and Paul, A.(1987), "Spatial localization in NMR spectroscopy in vivo," *Annals of the New York Academy of Sciences*, 508(1), 333-348.
- [11] Lim, A. K., Hamilton, G., Patel, N., Jimmy, J. D. and Taylor-Robinson, S. D.(2013), "¹H MR spectroscopy in the evaluation of

- the severity of chronic liver disease,” *Radiology*, 226(1), 288-289.
- [12] Johnson, J. A., Walton, D. W., Sachinwalla, T., Thompson, C. H., Smith, K., Ruell, P. A., Stannard, S. R. and George, J.(2008), “Noninvasive Assessment of Hepatic Lipid Composition: Advancing Understanding and Management of Fatty Liver Disorders,” *Hepatology*, 47(5), 757-763.
- [13] Corbin, I. R., Furth, E. E., Pickup, S., Siegelman, E. S., and Delikatny, E. J.(2009), “In vivo assessment of hepatic triglycerides in murine non-alcoholic fatty liver disease using magnetic resonance spectroscopy,” *Biochimica et Biophysica Acta (BBA)-Molecular and Cell Biology of Lipids*, 1791(8), 757-763.
- [14] Provencher, S. W.(1982). “A constrained regularization method for inverting data represented by linear algebraic or integral equations,” *Computer Physics Communications*, 27(3), 213-227.
- [15] Provencher, S. W.(2014). “LCmodel & LCMgui User’s Manual,” *LCModel Version*, 6, 2-3.
- [16] Cavassila, S., Deval, S., Huegen, C., Van Ormondt, D., and Graveron-Demilly, D.(2000), “Cramer-Rao bound expressions for parametric estimation of overlapping peaks: influence of prior knowledge,” *Journal of Magnetic Resonance*, 143(2), 311-320.
- [17] Cho, S. G., Kim, M. Y., Kim, H. J., Kim Y. S., Choi, W., Shin, S. H., Hong, K. C., Kim Y. B., Lee, J. H. and Suh, C. H.(2001), “Chronic hepatitis: in vivo proton MR spectroscopic evaluation of the liver and correlation with histopathologic findings,” *Radiology*, 221(3), 740-746.
- [18] Van Werven, J. R., Schreuder, T. C, M, A., Nederveen, A. J., Lavini. C., Jansen, P. L. M. and Stoker, J.(2010), “Hepatic unsaturated fatty acids in patients with non-alcoholic fatty liver disease assessed by 3.0T MR spectroscopy.” *Journal of lipid research*, 75(2), e102-e107.
- [19] Lee, Y. J., Jee, H. J., Noh, H. J., Kang, G. H., Park, J. Y., Cho, J. G., Cho, J. H., Ahn, S. D., Lee, C. H., Kim, O. H., Oh, B. C. and Kim, H. J.(2013), “In Vivo ¹H-MRS Hepatic Lipid Profiling in Nonalcoholic Fatty Liver Disease: An Animal Study at 9.4T,” *Magnetic resonance in medicine*, 70(3), 620-629.
- [20] Wang, D., Wei, Y. and Pagliassotti, M. J.(2006), “Saturated fatty acids promote endoplasmic reticulum stress and liver injury in rats with hepatic steatosis,” *Endocrinology*, 147(2), 943-951.
- [21] Cheung, J. S. Fan, S. J., Gao, D. S., Chow, A. M., Yang, J., Man, K. and Wu, E. X.(2011), “In vivo lipid profiling using proton magnetic resonance spectroscopy in an experimental liver fibrosis model,” *Academic Radiology*, 18(3), 377-383

Intrinsic apoptotic pathway and G2/M cell cycle arrest involved in tubeimoside I-induced EC109 cell death

^{1*}Yang Xu, ¹Guanghai Wang

Article in Chinese Journal of Cancer Research · June 2013

DOI: 10.3978/j.issn.1000-9604.2013.06.03 · Source: PubMed

©The Author(s) 2021

Abstract Squamous esophageal carcinoma is highly prevalent in developing countries, especially in China. Tu Bei Mu (TBM), a traditional folk medicine, has been used to treat esophageal squamous cell carcinoma (ESCC) for a long term. tubeimoside I (TBMS1) is the main component of TBM, exhibiting great anticancer potential. In this study, we investigated the mechanism of TBMS1 cytotoxic effect on EC109 cells. Comparative nuclear proteomic approach was applied in the current study and we identified several altered protein spots. Further biochemical studies were carried out to detect the mitochondrial membrane potential, cell cycle and corresponding proteins' expression and location. Subcellular proteomic study in the nucleus from EC109 cells revealed that altered proteins were associated with mitochondrial function and cell proliferation. Further biochemical studies showed that TBMS1-induced molecular events were related to mitochondria-induced intrinsic apoptosis and P21-cyclin B1/cdc2 complex-related G2/M cell cycle arrest.

Considering the conventional application of TBM in esophageal cancer, TBMS1 therefore may have a great potential as a chemotherapeutic drug candidate for ESCC.

Key Words: Anticancer drug; G2/M cell cycle arrest; intrinsic apoptosis; subcellular proteomics and tubeimoside I (TBMS1)

I. INTRODUCTION

Esophageal cancer (EC) is one of the most lethal cancers and ranks as the sixth leading cause of cancer-related death throughout the world (1). EC, arising from the inner layer of esophagus, represents two histological subtypes, including esophageal squamous cell carcinoma (ESCC) and esophageal adenocarcinoma (EAC) (2). Generally, most of EC in developing countries is ESCC, while EAC is more often in Western countries, which has the distinguishing etiologies and results in different therapeutics and prognosis. Moreover, ESCC is the major predominant cancer of esophagus, accounting for more than 90% of diagnosed cases, especially in China (3). Although multimodal therapies and the optimal approaches are still controversial issues, chemotherapy or chemoradiotherapy is also applied widely in clinic, particularly in unresectable EC (1).

^{1*}Yang Xu (✉)

School of Pharmaceutical Sciences, Xiamen University,
Xiamen 361005, China

The tuber of *Bolbostemma paniculatum* (Maxim.) Franquet (Cucurbitaceae), Chinese name as Tu Bei Mu (TBM), is a traditional folk medicine, and due to the heat and toxin clearing action, it has been applied in the treatment of mastitis, breast abscess, tubercular lymphadenitis and cancers, especially EC. Tubeimoside I (TBMS1) (Figure 1), a triterpenoid saponin, is the main component of TBM with anticancer activity. However, the detailed mechanisms and intracellular targets underlying TBMS1-induced EC cells toxicity remain elusive.

Mitochondrion is a key organelle inducing cell apoptosis in many tumor treatments. Increasing investigations have found that mitochondrial dysfunction is an effective way to suppress tumor progression, and numerous anticancer drugs

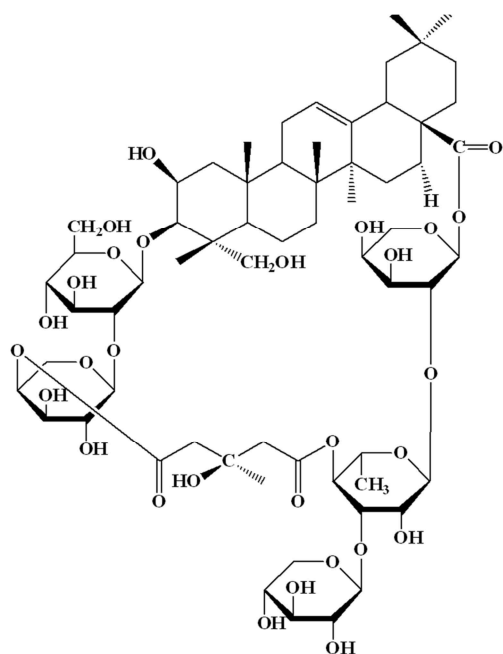


Figure 1 Chemical structure of TBMS1

evoke cancer cell death through mitochondrial dysfunction. The classical mitochondria-related apoptosis is to transport death signals via Bcl-2 family proteins, leading depletion of outer membrane potential, release of proteins residing in mitochondrial intermembrane space (MIS) and

activation of caspase cascade (4). The proteins leaking out from the MIS include cytochrome c, endonuclease G and apoptosis inducing factor (AIF) (5).

Deregulation of cell cycle regulators in different levels is detected in many human cancers. At the same time, cell cycle checkpoints are usually the potential anticancer chemotherapeutic targets. There are two conversed types of anticancer agents evoked by G2/M checkpoint deregulation (6). One affects the abrogation of G2/M checkpoint, making the damaged cells to mitosis stage and further inducing apoptosis (7). Another way is to promote the G2/M checkpoint, subsequently inducing apoptosis (8). Increasing evidence showed that many anticancer compounds trigger apoptosis, accompanying G2/M cell cycle arrest.

In the present study, we applied proteomics approach to predict the cytotoxicity mechanism of TBMS1 in ESCC cells (9). Our findings indicated that TBMS1 exhibited its cytotoxicity associated with mitochondrial dysfunction and G2/M cell cycle arrest. Further biochemical study revealed that caspase-3 and -9 were activated and AIF released. In addition, cyclin B/cdc2 complex and P21 were proved to play a critical role in TBMS1-induced EC109 cell G2/M arrest. Our findings may provide a rationale for the further investigation of TBMS1 in ESCC treatment.

II. Materials and methods

1. Materials

TBMS1 was purchased from National Institute for the Control of Pharmaceutical and Biological Products (China), dissolved in phosphate buffered saline (PBS) and stored at -20°C . JC-1 was purchased from Molecular Probes (Invitrogen, CA, USA). 4',6-diamidino-2-phenylindole (DAPI) was brought from Roche (Mannheim, Germany).

Subcellular proteome extract kit (S-PEK) was obtained from CalBiochem (San Diego, CA, USA). All other chemicals, except otherwise noted, were purchased from Sigma.

2. Cell culture and treatment

EC109 cells were cultured in DMEM (High Glucose) supplemented with 10% fetal bovine serum (FBS) under standard culture condition. At 80% confluence, cultures were treated with desired TBMS1 for cell growth and cell cycle analysis.

3. Cytotoxicity assay

Cytotoxicity was evaluated by MTT assay. Cells were suspended at 1×10^4 cells/well and 200 μ L of suspension was plated onto each well of a 96-well plate. After 24 h, the medium was replaced by various concentrations of TBMS1. At the end of treatment, the medium was removed, and 20 μ L 5 mg/mL MTT in DMEM medium was added. The cells were further incubated in 5% CO₂ at 37 °C for 4 h. Formazan was solubilized with 100 μ L dimethylsulfoxide (DMSO) and measured at 595 nm.

4. Colony formation efficiency analysis

The assay was performed in 6-well plates with a bottom layer containing 0.6% agar in DMEM containing 20% FBS. Cells were seeded at a concentration of 5,000/mL in top layer with 0.3% agar, 20% FBS, and treated with desired doses of TBMS1. The plates were incubated at 37 °C for 14 d and the medium with or without TBMS1 was changed every three days. The number of colonies was counted with a microscope and showed as $\bar{x} \pm s$ with three independent assays.

5. DNA laddering

DNA laddering was analyzed by Lei's protocol (9). Equal DNA extractions from treated or untreated

EC109 cells were run on 1% agarose gel, and bands were detected by ethidium bromide staining.

6. Flow cytometry analysis of cell cycle distribution

EC109 cells were treated with desired doses of TBMS1 for 24 h. At the end of each experiment, 1×10^6 EC109 cells were harvested, stained with propidium iodide (PI) and evaluated by FACStar Plus flow cytometer. Cell cycle was distributed via the WinMDI 2.9 software.

7. Confocal microscopic analysis

EC109 cells were attached on cover slips and then exposed to TBMS1 for indicated time. Corresponding primary and fluorescein isothiocyanate (FITC)-conjugated secondary antibodies were used to stain the specific proteins. DAPI was used to stain the nucleus (blue). Mito Tracker red (Molecular Probes, Invitrogen) was performed to dye mitochondria. Corresponding primary and FITC-conjugated secondary antibodies were used to stain AIF and P21 proteins (green). Confocal laser-scanning immunofluorescent microscopy analysis was applied on Zeiss LSM510 Confocal Microscope System (Carl Zeiss, Thornwood, NY).

8. Two-dimensional electrophoresis (2-DE) and mass spectrometry (MS) analysis

2-DE was performed with GE IPGphor IEF and Ettan Dalt Six electrophoresis units by following protocol described previously. Image analysis was carried out with the ImageMaster 2D Elite software (GE Healthcare, UK). Only those protein spots showing reproducible alterations in three independent experiments (over 2.0-fold up- or down-regulation) were selected for tryptic in-gel digestion and MS analysis. Peptide mass spectra were obtained on an ABI 4800-plus MALDI TOF/TOF mass spectrometer

in a reflector positive ion mode with average 1,500 laser shots per spectrum. Peptide ion masses were internally calibrated using trypsin autolytic peptides at m/z 842.51 and 2,211.10. TOF/TOF tandem MS fragmentation spectra were acquired in a data-dependent fashion based on the MALDI-TOF peptide mass map for each protein, and 10 most abundant ions present were selected in each sample (excluding trypsin autolytic peptides and other known background ions). All these data were processed by using the GPS Explorer software (V3.6, Applied Biosystems). MASCOT was used in searching for protein identification by NCBI protein database. The mass tolerance was set at 75 ppm. Species search was limited to human.

9. Western immunoblotting

Total cell lysates were denatured with sample loading buffer and then subjected to sodium dodecyl sulfate-polyacrylamide gel electrophoresis (SDS-PAGE) for protein separation. After transferred onto membranes, the proteins were probed with corresponding antibodies and detected by ECL detection reagents (GE, UK). The primary antibodies for cdc2, PARP and P21 were purchased from Cell Signaling (Beverly, MA, USA). Primary antibodies for cyclin B1, Bcl-2 and Bax were purchased from Santa Cruz Biotechnology (Santa Cruz, CA, USA). Anti-cdc2 was from Abcam. Antibodies for β -actin and secondary anti-mouse and rabbit antibodies were from Sigma (USA).

10. Statistical analysis

Statistical analysis was done through Excel data analysis using a two tailed Student's t -test and $P < 0.05$ was considered statistically significant. Data are expressed as $\bar{x} \pm s$ of triplicate samples, and the reproducibility was confirmed in three separate experiments.

III. Results

1. EC109 cells show apoptotic characteristics with TBMS1 treatment

After treatment with indicated concentration of TBMS1 (Figure 1) for 24 or 48 h, we concluded that IC₅₀ of TBMS1 to EC109 was almost 45 and 35 $\mu\text{mol/L}$ at 24 and 48 h, respectively (Figure 2A,B). DNA laddering was analyzed after 30 and 45 $\mu\text{mol/L}$ TBMS1 administration for 12 h in EC109 cells. The degradation of cellular DNA elevated in a dose-dependent manner (Figure 2C). In addition, typical apoptotic morphological changes of EC109 cells were detected by DAPI staining (Figure 2D). In Figure 2D, TBMS1-induced chromatin condensation was clearly detectable after TBMS1 treatment and a large amount of apoptotic bodies particularly appeared after 24 h. The percentage of apoptotic cells increased by about 13% and 40% over untreated EC109 cells, after 30 and 45 $\mu\text{mol/L}$ TBMS1 treatment for 24 h, respectively. All above data implicated that TBMS1 induced obvious apoptosis in EC109 cells.

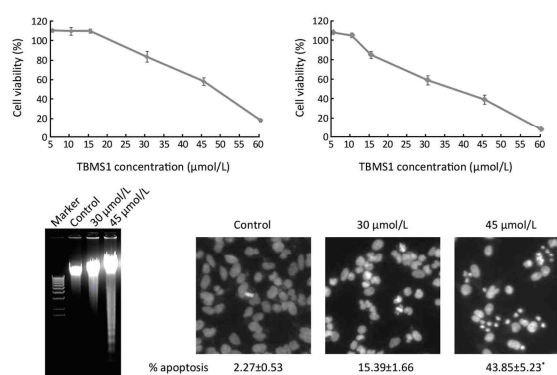


Figure 2 The cytotoxicity induced by TBMS1 in EC109. Concentration dependence of TBMS1 cytotoxicity on EC109 cells with 24 h (A) or 48

h (B) treatment. C. DNA ladder was formed after TBMS1 treatment for 12 h at indicated concentrations (representative from three independent experiments); D. The cells were stained by DAPI and visualized by fluorescent microscope at indicated time; the values are listed as $\bar{x} \pm s$ of triplicate experiments ($\times 320$); *, $P < 0.05$ compared with untreated EC109 cells

2. Cellular proteins alter in response to TBMS1 administration

S-PEK kit was used to separate the total proteins from EC109 into mainly 3 different parts, including cytoplasm, membrane and nucleus fractions (Figure 3A). Figure 3A shows the representative 2-DE images for nuclear proteins extracted from EC109 cells treated and untreated with 45 $\mu\text{mol/L}$ TBMS1 for 24 h. More than 1,000 protein spots were detected from MW 6-200 kDa and pI 3-10. The altered spots were exhibited in Figure 3B. The spots with great differences (up- or down-regulation over 2-fold) were selected to run MS. Finally, we identified 10 proteins and their spot number, ID, MW/pI values, fold difference, scores and main function are listed in Table 1. These altered proteins are up-regulation of prohibitin (PHB), Tu translation elongation factor, mitochondrial (TUFM) and annexin A2; and down-regulation of β -tubulin, γ -actin, heterogeneous nuclear ribonucleoprotein K (HNRNPK), nucleophosmin 1 (NPM1), lamin B2 (LMNB2), aldolase A and histone H1.

TBMS1 causes mitochondrial dysfunction

Considering that mitochondria were a kind of important organelles initiating apoptosis and proteomic changes related to glycolytic enzyme and mitochondrial stress, we further evaluated the function and corresponding markers of mitochondria-associated proteins. The activity of caspase-3 and caspase-9 was firstly estimated (Figure 4A). Then, mitochondrial transmembrane potential ($\Delta\Psi\text{m}$) was

measured to detect the mitochondrial integrity by JC-1 staining (Figure 4B). The activation of caspase-3 and caspase-9 was observed upon TBMS1 treatment with different concentrations and the depletion of $\Delta\Psi\text{m}$ exhibited apparently under 45 $\mu\text{mol/L}$ TBMS1 for 6 h.

The mitochondrial cell death pathway is regulated by Bcl-2 family. Particularly, the ratio of Bax (pro-apoptotic member) to Bcl-2 (antiapoptotic member) is critical for MIS molecule release and the following caspase activation. Western blot analysis indicated that increased Bax expression was concurrent with suppressed Bcl-2 in a dose-dependent manner (Figure 4C). In addition, fluorescent analysis of AIF revealed that after 45 $\mu\text{mol/L}$ TBMS1 exposure for 12 h, AIF released from mitochondria to cytoplasm, even into nucleus (Figure 4D). These results confirmed that TBMS1 evoked mitochondrial dysfunction-related apoptosis in EC109 cells.

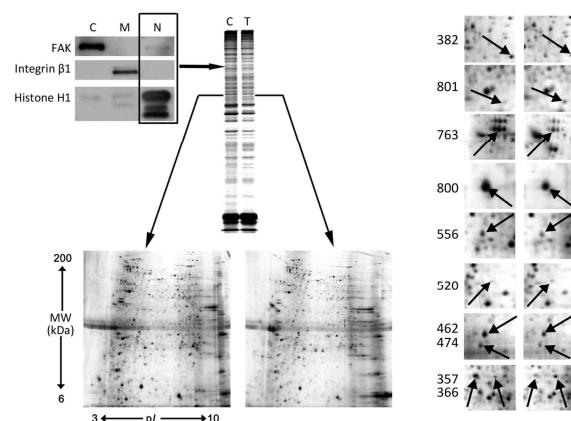


Figure 3 2-DE analysis of subcellular proteomic from nuclear fractionation of EC109 cells after TBMS1 administration. A. Western blotting against protein markers for cytosolic (C), membrane (M) and nucleic (N) protein fractions (C, control; T, TBMS1 treatment). After treated or untreated with 45 $\mu\text{mol/L}$ TBMS1 for 24 h, representative 1-DE and 2-DE images from three independent experiments for nuclear proteins extracted from EC109 cells were exhibited; B. The interested altered protein spots of nuclear proteins from EC109 cells were identified by

MS

The mitochondrial cell death pathway is regulated by Bcl-2 family. Particularly, the ratio of Bax (proapoptotic member) to Bcl-2 (antiapoptotic member) is critical for MIS molecule release and the following caspase activation. Western blot analysis indicated that increased Bax expression was concurrent with suppressed Bcl-2 in a dose-dependent manner (Figure 4C). In addition, fluorescent analysis of AIF revealed that after 45 $\mu\text{mol/L}$ TBMS1 exposure for 12 h, AIF released from mitochondria to cytoplasm, even into nucleus (Figure 4D). These results confirmed that TBMS1 evoked mitochondrial dysfunction-related apoptosis in EC109 cells.

Table 1. Protein alterations related to cell growth regulation in response to TBMSI exposure(25 $\mu\text{mol/L}$ for 24 h)

Spot No.	Protein ID	MW (kDa)/pI	Difference ($\Delta\pm s$)	Score/CI %	Peptide count
801	Prohibitin (PHB)	30.0/5.57	+3.13 \pm 0.5	356/100	6
382	β -tubulin	49.6/4.75	-2.83 \pm 0.36	250/100	12
357	HNRNPK	50.9/5.39	-3.33 \pm 0.43	133/100	15
366	TUFM	49.8/7.26	-2.74 \pm 0.24	120/100	11
763	NPM1	32.6/4.64	-4.27 \pm 0.38	88/99.98	6
462	LMNB2	69.9/5.50	-3.84 \pm 0.54	150/100	9
474	actin, gamma 1	41.8/5.31	-3.74 \pm 0.61	121/100	7
556	Aldolase A	39.4/8.30	-2.13 \pm 0.32	235/100	14
520	Annexin A2	38.0/7.57	+2.03 \pm 0.4	118/100	8
800	Histone H1	23.7/11.58	-2.22 \pm 0.31	96/99.98	8

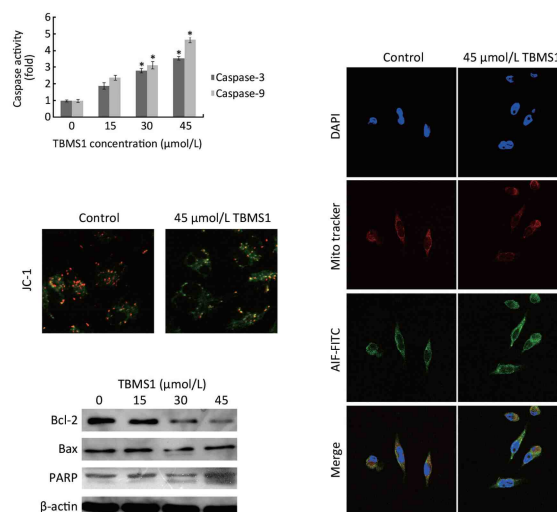


Figure 4 Mitochondrial dysfunction induced by TBMS1 in EC109 cells. A. The activation of caspase-3 and -9 was evaluated by caspase activity kit after indicated concentration of TBMS1 treatment for 6 h; *, $P < 0.05$ compared with untreated EC109 cells; B. Mitochondrial transmembrane potential ($\Delta\Psi_m$) was measured with JC-1 staining under 45 $\mu\text{mol/L}$ TBMS1 for 6 h; C. Western blotting detected the proteins of Bcl-2, Bax and PARP-1 after 24 h TBMS1 treatment; D. Fluorescent analysis of AIF revealed after 45 $\mu\text{mol/L}$ TBMS1 exposure for 12 h. All these results are representative from three independent experiments

3. Modulation of G2/M cell cycle regulators by TBMS1

Proteomic alteration also gave us a clue that TBMS1 affects the proliferation of EC109. The soft agar colony formation assay was applied to monitor anchorage-independent growth, measuring proliferation in a semisolid culture media. In the present study, after TBMS1 treatment for 14 d, the number of colonies formed was significantly fewer than the untreated cells ($P < 0.001$) (Figure 5A). Figure 5A clearly shows that TBMS1 caused a concentration-dependent reduction of colony formation, with 54.7% and 21.9% colonies corresponding to the treatment with 30 and 45 $\mu\text{mol/L}$ TBMS1, respectively. Further, we detected the cell cycle distribution via flow cytometry. Figure 5B,C showed that the treatment with 45 $\mu\text{mol/L}$

TBMS1 for 12 and 24 h resulted in an increased population of G2/M phase cells, resulting in 15-24% cell increase in G2/M phase.

Three regulatory molecules, cyclin-dependent kinases (CDKs), cyclins and cyclin-dependent kinase inhibitors (CDKIs), determine the cell cycle progression by controlling the cell cycle. CDK-cyclin complexes are the ultimate target of cell cycle transition. Western blot analysis in *Figure 5D* showed a strong decrease of cdc2 and cyclin B1 in both cytoplasm and nucleus fraction. Other negative regulators of CDKs are a family of inhibitory proteins known as CDKIs, including Cip1/P21 and Kip1/ P27. Our results revealed that TBMS1 treatment caused a strong overexpression of Cip1/P21 in cytoplasm and nucleus (*Figure 5D*). We also detected the decrease of Cip1/ P21 with fluorescent analysis (*Figure 5E*), verifying that Cip1/P21 accumulated to the nucleus to interrupt the cell cycle progression. In this respect, our data suggest that TBMS1 affected cdc2/cyclin B1 complex pathway and P21 expression and location, contributing to the G2/M arrest.

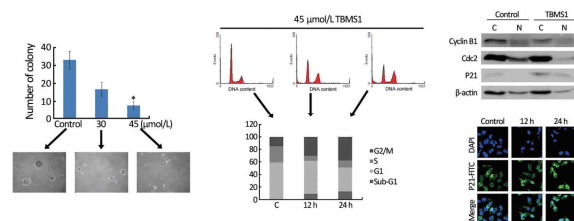


Figure 5 Effect of TBMS1 on EC109 cell cycle distribution. A. EC109 cells were incubated with increasing concentrations of TBMS1 for 14 d and then the number of colonies was counted; *, $P < 0.05$ compared with untreated EC109 cells; B,C. An increased population of G2/M phase cells was evoked after treatment with 45 $\mu\text{mol/L}$ TBMS1 for 12 and 24 h; D. Western blotting detected the proteins of cyclin B1, cdc2 and P21 in cytosol and nucleus fractions after 45 $\mu\text{mol/L}$ TBMS1 administration for 24 h; E, Immunocytochemical analysis for the cytoplasmic and nuclear localization of P21 after 12 and 24 h treatment with 45 $\mu\text{mol/L}$

TBMS1 by confocal microscope

IV. Discussion

TBM is the key herb constituent in the Chinese folk medicine to treat cancer for thousands of years. Numerous evidences indicated that TBMS1 is the crucial component of TBM with anticancer effect on several cancer cell lines. Especially, our previous results demonstrated that TBMS1 could induce death of HeLa, HepG2, A549 and HL-60 cells (data not shown). In addition, earlier reports demonstrated that TBMS1 has low toxicity *in vitro* and *in vivo* (10). This conclusion coincided with that triterpenoid saponins extracted from traditional Chinese herbal medicines have been shown low cytotoxicity to normal cells. Particularly, based on a long term clinical experience in traditional Chinese herb medicine for EC treatment, we suggested that TBMS1 could be used in chemotherapy and has low toxicity. Because ECSS is a main subtype of EC in China, here we choose EC109 as the cell model. In the present investigation, the evaluation of the mechanism underlying TBMS1-induced EC109 cell death could contribute to the development of TBMS1 as a promising anticancer agent in ECSS treatment.

From previous results, we have known that there is a broad spectrum of carcinoma cell species for TBMS1-induced cytotoxicity, including HeLa, A549, HL-60, SGC- 7901, PC-3 and Bel-7402 (11). Here, we examined the effect on EC109, showing the dose- and time-dependent cytotoxicity. Then, we evaluated TBMS1-induced alteration of nucleus morphology and DNA fragmentation, which indicated TBMS1-associated apoptosis. To give an insightful understanding of TBMS1's effects on EC109, nuclear comparative proteomic analysis was further carried out. Compared to the total protein profiling, this method will reveal more detailed information

from nucleus, implicating several involved cell signaling pathways. The altered spots proteins are listed in details as follows.

LMNB2 is believed to be critical for eukaryotic cells in DNA replication and in the formation of the mitotic spindle. The absence or down-regulation of LMNB2 in HeLa cells was demonstrated to arrest cell growth and lead to apoptosis (12). β -tubulin is one of the essential components of microtubule and its dynamic alteration has been proposed as a target of anticancer drugs, inducing mitotic arrest of cells in the G2/M stage (13). HNRNPK belongs to the subfamily of ubiquitously expressed heterogeneous nuclear ribonucleoproteins (hnRNPs). Several experiments verified that HNRNPK acted as a cofactor for P53 in response to DNA damage (14-16). Knockdown of HNRNPK by siRNA inhibited pancreatic cancer cell growth and colony formation, implying its function during cell cycle progression (15).

Of note, all these altered proteins in current study are located in nucleus; however, most of them participate in the integration cell signaling process between nucleuses and cytoplasm or mitochondria, such as TUFM, NPM1, PHB, aldolase A and annexin A2. TUFM plays a central role in protein translation in mitochondria. Thus, in our experiment, down-regulation of TUFM will directly influence on the synthesis of mtDNA-encoded proteins, implicating the mitochondrial damage. Moreover, over-expression of TUFM was proved to rescue mitochondrial dysfunction (17) and ShRNA-mediated knockdown of TUFM in leukemic cells exhibited the similar outcome to the interrupted mitochondrial translation and antileukemia activity (18). NPM1 is multifunctional nuclear acidic chaperone, which moves between the nucleus and the cytoplasm involving in several processes, including ribosome biogenesis, chromatin remodeling, and mitosis as well as in DNA repair, replication and

transcription (19). Expression of NPM1 is weak in normal hepatocytes and has an obvious positive correlation with the increased tumor grading and poor prognosis (20). In addition, suppression of NPM1 expression was found to enhance adriamycin chemosensitivity in adriamycin-resistant human gastric cancer cell line (21). NPM1 also plays an important role in the regulation of the alternate reading frame (ARF)-P53 tumor-suppressor pathway (22). PHB is an evolutionary conserved protein, involved in the regulation of cell growth, proliferation, differentiation, aging, and apoptosis (23,24). It was initially believed to be a chaperone with tumor suppression function that resides in the mitochondrial inner membrane (25); however, increasing evidence revealed that PHB also located in nuclear matrix and carried out its function through being exported from the nucleus to the mitochondria (26). Accumulation of PHB in nucleus may reflect the unsuccessful translocation to mitochondria and dysfunction of mitochondria. Aldolase A is a glycolytic enzyme, existing both in nucleus and cytoplasm (11), even in mitochondrial fraction (11). Knockdown of aldolase A in Ras-transformed NIH-3T3 cells causes inhibition of the cell proliferation, whereas it could be recovered by exogenous aldolase A. Accordingly, knockdown of aldolase A by RNAi was indicated as a potential therapeutic target for cancer treatment (27). Annexin A2 is a pleiotropic protein and plays its role depending on its different location. It involved in diverse cellular processes such as cell motility, endocytosis, cell proliferation, apoptosis and cytoskeleton reorganization (11). Some evidence shows that annexin A2 could interact with PHB for its function (28).

Therefore, based on the above analysis, these proteins mainly contributed to abnormal mitochondrial function and cell proliferation inhibition. Consequently, mitochondria-related function and TBMS1-induced cell proliferation were

further evaluated.

Disruption of mitochondrial transmembrane potential and the elevated caspase-9 and -3 activities (*Figure 5A,B*) provided a powerful hints that intrinsic apoptotic pathway was involved in TBMS1-related EC109 cytotoxicity. The intrinsic apoptotic pathway is initiated mainly by the dysfunction of mitochondria, which is regulated via the Bcl-2 family proteins. In our current study, the apparently increased ratio of Bax to Bcl-2 and the cleaved-PARP confirmed the mitochondria-initiated intrinsic apoptosis. In addition, after mitochondrial transmembrane damage, cytochrome c, Smac/DIABLO and AIF would release from the MIS. Especially, AIF, a mitochondrial flavoprotein, leaked out from MIS, and then translocated from cytoplasm to nucleus during apoptosis, finally leading to chromatin condensation and large scale DNA fragmentation independent of caspases (4,29-31). Therefore, our results implied that TBMS-1 induced mitochondrial intrinsic apoptosis through caspase-dependent and -independent pathways.

Next, we focused on the TBMS1-mediated proliferation and cell growth. TBMS1 inhibited the proliferation of EC109 and arrested the cells in the G2/M phase. Furthermore, we found the increased population of G2/ M cells has a great positive relation with elevated apoptotic population (*Figure 5B*). The heterodimeric complex of cdc2 and cyclin B1 is the ultimate target of G2/M cell cycle. TBMS1 decreased cdc2 protein levels, with a concomitant decrease in cyclin B1 expression in EC109 cells, both in cytoplasm and nucleus fractions.

Besides cyclin and CDK complex, CDKIs are the other key regulators in the cell cycle progression. P21 is not only the principal mediator of G1-phase arrest in response to DNA damage (32), but also participates in the maintenance of cells in G2/M phase through multiple mechanisms (33). Although P21 has a relatively low affinity to cyclin B1-cdc2

complex, it has been demonstrated to contribute to cdc2 inactivation by inhibiting the cdc2 phosphorylation at Thr161 to enforce the G2/M DNA damage checkpoint (34). In current study, P21 was observed not only elevated expression, but also translocated to nuclear (*Figure 5D,E*), which further demonstrated its function on cyclin B1 and cdc2 complex.

In this project, we explored the alteration of nuclear proteins after TBMS1 exposure to EC109. From the identified protein, mitochondrial dysfunction and cell cycle arrest were speculated to involve in the process of TBMS1- mediated EC109 cell death. Further functional studies demonstrated that TBMS1-induced apoptosis is through mitochondrial intrinsic apoptosis and P21-cdc2/cyclin B1 signaling pathway. In addition, mitochondria-nucleus communication in TBMS1-induced EC109 cytotoxicity excites our attention, and it may be the main role in this process and deserved further investigation.

[References]

1. Schweigert M, Dubecz A, Stein HJ. Oesophageal cancer-an overview. *Nat Rev Gastroenterol Hepatol* 2013;10:230-44.
2. Pennathur A, Gibson MK, Jobe BA, et al. Oesophageal carcinoma. *Lancet* 2013;381:400-12.
3. Metzger R, Schneider PM, Warnecke-Eberz U, et al. Molecular biology of esophageal cancer. *Onkologie* 2004;27:200-6.
4. Zhai D, Jin C, Huang Z, et al. Differential regulation of Bax and Bak by anti-apoptotic Bcl-2 family proteins Bcl-B and Mcl-1. *J Biol Chem* 2008;283:9580-6.
5. Wang X. The expanding role of mitochondria in apoptosis. *Genes Dev* 2001;15:2922-33.
6. DiPaola RS. To arrest or not to G(2)-M Cell-cycle arrest : commentary re: A. K. Tyagi et al.,

- Silibinin strongly synergizes human prostate carcinoma DU145 cells to doxorubicin-induced growth inhibition, G₂-M arrest, and apoptosis. *Clin Cancer Res* 2002;8:3311-4.
7. Kawabe T. G₂ checkpoint abrogators as anticancer drugs. *Mol Cancer Ther* 2004;3:513-9.
 8. Weir NM, Selvendiran K, Kutala VK, et al. Curcumin induces G₂/M arrest and apoptosis in cisplatin-resistant human ovarian cancer cells by modulating Akt and p38 MAPK. *Cancer Biol Ther* 2007;6:178-84.
 9. Lei T, He QY, Cai Z, et al. Proteomic analysis of chromium cytotoxicity in cultured rat lung epithelial cells. *Proteomics* 2008;8:2420-9.
 10. Yu L, Ma R, Wang Y, et al. Potent anti-tumor activity and low toxicity of tubeimoside 1 isolated from *Bolbostemma paniculatum*. *Planta Med* 1994;60:204-8.
 11. Yin Y, Chen W, Tang C, et al. NF- κ B, JNK and p53 pathways are involved in tubeimoside-1-induced apoptosis in HepG2 cells with oxidative stress and G₂/M cell cycle arrest. *Food Chem Toxicol* 2011;49:3046-54.
 12. Steen RL, Collas P. Mistargeting of B-type lamins at the end of mitosis: implications on cell survival and regulation of lamins A/C expression. *J Cell Biol* 2001;153:621-6.
 13. Eisenlöffel C, Schmöle AC, Pews-Davtyan A, et al. Interference of a novel indolylmaleimide with microtubules induces mitotic arrest and apoptosis in human progenitor and cancer cells. *Biochem Pharmacol* 2013;85:763-71.
 14. Pelisch F, Pozzi B, Risso G, et al. DNA damage-induced heterogeneous nuclear ribonucleoprotein K sumoylation regulates p53 transcriptional activation. *J Biol Chem* 2012;287:30789-99.
 15. Zhou R, Shanas R, Nelson MA, et al. Increased expression of the heterogeneous nuclear ribonucleoprotein K in pancreatic cancer and its association with the mutant p53. *Int J Cancer* 2010;126:395-404.
 16. Lee SW, Lee MH, Park JH, et al. SUMOylation of hnRNP-K is required for p53-mediated cell-cycle arrest in response to DNA damage. *EMBO J* 2012;31:4441-52.
 17. Feuermann M, Francisci S, Rinaldi T, et al. The yeast counterparts of human 'MELAS' mutations cause mitochondrial dysfunction that can be rescued by overexpression of the mitochondrial translation factor EF-Tu. *EMBO Rep* 2003;4:53-8.
 18. Skrtić M, Sriskanthadevan S, Jhas B, et al. Inhibition of mitochondrial translation as a therapeutic strategy for human acute myeloid leukemia. *Cancer Cell* 2011;20:674-88.
 19. Lindström MS. NPM1/B23: A Multifunctional Chaperone in Ribosome Biogenesis and Chromatin Remodeling. *Biochem Res Int* 2011;2011:195209.
 20. Liu X, Liu D, Qian D, et al. Nucleophosmin (NPM1/ B23) interacts with activating transcription factor 5 (ATF5) protein and promotes proteasome- and caspase-dependent ATF5 degradation in hepatocellular carcinoma cells. *J Biol Chem* 2012;287:19599-609.
 21. Yang YX, Hu HD, Zhang DZ, et al. Identification of proteins responsible for the development of adriamycin resistance in human gastric cancer cells using comparative proteomics analysis. *J Biochem Mol Biol* 2007;40:853-60.
 22. Cazzaniga G, Dell'Oro MG, Mecucci C, et al. Nucleophosmin mutations in childhood acute myelogenous leukemia with normal karyotype. *Blood* 2005;106:1419-22.
 23. Shi SL, Li QF, Liu QR, et al. Nuclear matrix protein, prohibitin, was down-regulated and translocated from nucleus to cytoplasm during the differentiation of osteosarcoma MG-63 cells

- induced by ginsenoside Rg1, cinnamic acid, and tanshinone IIA (RCT). *J Cell Biochem* 2009;108:926-34.
24. Sripathi SR, He W, Atkinson CL, et al. Mitochondrial-nuclear communication by prohibitin shuttling under oxidative stress. *Biochemistry* 2011;50:8342-51.
25. Merkwirth C, Langer T. Prohibitin function within mitochondria: essential roles for cell proliferation and cristae morphogenesis. *Biochim Biophys Acta* 2009;1793:27-32.
26. Rastogi S, Joshi B, Fusaro G, et al. Camptothecin induces nuclear export of prohibitin preferentially in transformed cells through a CRM-1-dependent mechanism. *J Biol Chem* 2006;281:2951-9.
27. Ritterson Lew C, Tolan DR. Targeting of several glycolytic enzymes using RNA interference reveals aldolase affects cancer cell proliferation through a non-glycolytic mechanism. *J Biol Chem* 2012;287:42554-63.
28. Bacher S, Achatz G, Schmitz ML, et al. Prohibitin and prohibitone are contained in high-molecular weight complexes and interact with alpha-actinin and annexin A2. *Biochimie* 2002;84:1207-20.
29. Pasupuleti N, Leon L, Carraway KL 3rd, et al. 5-Benzylglyciny-amiloride kills proliferating and nonproliferating malignant glioma cells through caspase-independent necroptosis mediated by apoptosis-inducing factor. *J Pharmacol Exp Ther* 2013;344:600-15.
30. Cregan SP, Dawson VL, Slack RS. et al. Role of AIF in caspase-dependent and caspase-independent cell death. *Oncogene* 2004;23:2785-96.
31. Candé C, Cohen I, Daugas E, et al. Apoptosis-inducing factor (AIF): a novel caspase-independent death effector released from mitochondria. *Biochimie* 2002;84:215-22.
32. Cheng MH, Yang YC, Wong YH, et al. B1, a novel topoisomerase II inhibitor, induces apoptosis and cell cycle G1 arrest in lung adenocarcinoma A549 cells. *Anticancer Drugs* 2012;23:191-9.
33. Choi YK, Seo HS, Choi HS, et al. Induction of Fas-mediated extrinsic apoptosis, p21WAF1-related G2/M cell cycle arrest and ROS generation by costunolide in estrogen receptor-negative breast cancer cells, MDA-MB-231. *Mol Cell Biochem* 2012;363:119-28.
34. Smits VA, Klompmaaker R, Vallenius T, et al. p21 inhibits Thr161 phosphorylation of Cdc2 to enforce the G2 DNA damage checkpoint. *J Biol Chem* 2000;275:30638-43.

Spatial Frequency Analysis by DWT of CXR in the COVIDGR Dataset

¹Giljae Lee,^{2,*}Gyehwan Jin, ¹Taesoo Lee

Received : 20 July 2021 / Accepted : 15 November 2021 / Published online: 28 December 2021

©The Author(s) 2021

Abstract In this study, chest X-ray images from the “COVIDGR Dataset” were formalized, and both normal images and disease severity images (mild, moderate, and severe) were extracted by the discrete wave transform (DWT) method. The characteristics of Approximation, Horizontal, Vertical, and Diagonal were analyzed as normal, mild, and vector frequencies. The standardized pixel was a format of 512 x 512 images and was intended to include all lung fields, except the original image did not include the apex of the lung. The standardized images were extracted by DWT for the characteristics of Approximation, Horizontal, Vertical, and Diagonal and stored as COVIDGR-19 Feature Data. These data were entered into an Excel file to calculate the sum, and the average value was obtained and confirmed as the “Feature value of images by disease.” Experiments showed that images of severe disease had little or no Approximation, high Diagonal content, and similarity between the Horizontal and Vertical characteristics. Normal images had the largest proportion of Approximation because there was no change in frequency due to the absence of disease, while mild and moderate images were similar in Approximation, Horizontal, and Vertical but had a one-sided bias in small areas for Diagonal. It is hoped that the results of this study can be used as an important parameter in an automatic identification system of chest X-ray images to allow timely diagnosis of patients with COVID-19 and other lung conditions.

Key words: COVID-19, Chest X-ray, DWT, Feature extraction, Machine learning

I. Introduction

The World Health Organization (WHO) declared a global pandemic [1] on March 11, 2020, after the coronavirus disease 2019 (COVID-19) epidemic in China spread beyond a specific regional window to more than two continents [2]. Since establishment of the WHO in 1948, only two other pandemics have been declared: the “Hong Kong Flu” pandemic in 1968, and the “Influenza A virus subtype H1N1” pandemic in 2009 [3].

An unknown respiratory epidemic began in December 2019, in Wuhan, China, and gradually spread to all regions and countries of the world. On January 9, 2020, the WHO declared that it was a new strain of coronavirus officially named COVID-19 [4]. Throughout 2020, the pandemic occurred in developed countries, such as continental Europe and the United States, as well as around the world, with a total of 81,997,998 infections and 1,789,927 deaths as of December 31, 2020. [5]. In 2021, the coronavirus developed mutations named Beta, Gamma, and Delta; Delta mutations became the

¹Giljae Lee,^{2,*}Gyehwan Jin(✉), ¹Taesoo Lee

¹Dept. of Biomedical engineering, Graduate school of Chungbuk National University, Chungbuk, Korea

^{2,*}Dept. of Radiology, Nambu University, Gwangju, Korea

predominant strain worldwide in the summer of 2021. Academic organizations are distributing research to overcome the COVID-19 pandemic, and universities, public research institutes, and pharmaceutical and biotechnology companies are working together to develop diagnostic methods, vaccines, and treatments. To date, diagnosis of COVID-19 has been verified using one of the three following methods [7]:

Computed tomography (CT)-based evaluation: Three-dimensional images obtained from various angles can be analyzed, but small medical institutions often do not have these devices available. CT also requires more than 15 minutes of testing and has the disadvantage of radiation exposure.

Reverse transcription polymerase chain reaction (RT-PCR) examination: RT-PCR is a method of detecting viral RNA in sputum or non-pharyngeal swab specimens. Specific materials and equipment frequently are not accessible, and testing requires 12 hours. This method has the limitation of needing an extended time for testing, which is not advantageous when positive patients must be identified as soon as possible. In addition, some studies have shown that RT-PCR results can produce false negatives in the same patient. If the RT-PCR test is positive, additional tests, such as CT scanning, might be required for confirmation.

Chest X-ray (CXR): A method that requires less auxiliary equipment, involves lighter equipment, and can be administered using mobile medical devices. In general, CXR testing is an easy way to assess patients prior to RT-PCR and CT-scan testing. CXR is the most efficient method of testing for COVID-19 in terms of both time and cost.

Automatic determination of medical images by machine learning requires images to be acquired in a form that is stereotyped by image acquisition equipment and data mining (i.e., preprocessing)

through feature extraction of acquired images [8]. It takes many steps to create models that incorporate pretreated image data (extracted feature values) and clinical data and to build an evidence-based decision tree.

In this study, the CXR images of the “COVIDGR Dataset” were formalized. Normal images and COVID-19 patient images (mild, moderate, and severe) were extracted by discrete wavelet transformation (DWT) to characterize the low-frequency region, horizontal high-frequency region, vertical high-frequency region, and diagonal high-frequency region. It is believed that the results of this study can be used as an important parameter for an automatic identification system of CXR images that will be available in the future.

II. Materials and methods

1. COVIDGR Dataset

The COVIDGR Dataset is part of a homogeneous and balanced database, COVIDGR-1.0, that includes positive RT-PCR patients who have been classified with mild, moderate, or severe COVID-19 and was developed in collaboration with the Hospital Universitario San Cecilio in Granada, Spain [8]. COVIDGR-1.0 contains 426 positive posteroanterior (PA) CXR images and 426 negative PA CXR images [7].

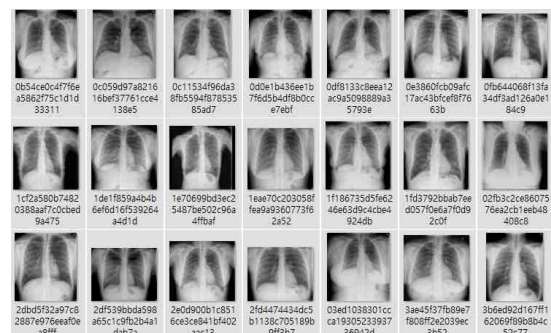


Figure 1. A sample of the negative (normal) images in the COVIDGR-1.0 Dataset

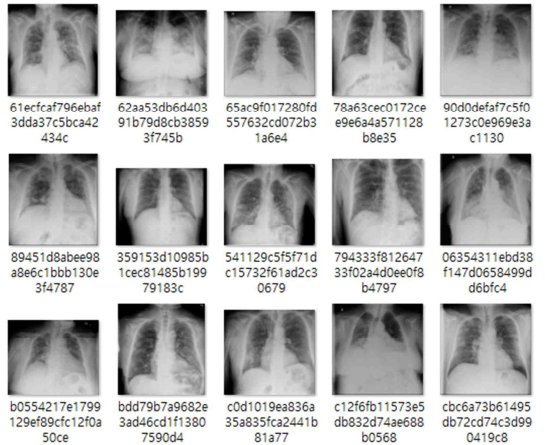


Figure 2. A sample of positive (severe) images in the COVIDGR-1.0 Dataset

2. Extracting characteristics of chest X-ray images

The Matlab wavelet toolbox was used to extract features of CXR images. A major challenge of wavelets is that time-frequency interpretation can be variable at the same time as the characteristics of Fourier’s interpretation of signals in the frequency domain. Because Fourier transforms do not have time information and cannot be used for time-frequency analysis, STFTs that introduce the time window concept for Fourier transforms are available. However, in the time-frequency analysis of STFT, there is no coherence of the underlying data, so sensitivity to singularity is reduced. Thus, a method to conduct a time-frequency analysis without compromising the topologicality of the base has been devised, which is the wavelet transformation [8]. The defining characteristics of time-frequency analysis by wavelet transformation are that the time resolution is high in the high-frequency domain and the frequency resolution is high in the low-frequency domain. Therefore, wavelet transformation is more

effective in time-frequency analysis than is STFT because the rapidly changing signal’s position at the time of the change is important, and the period or frequency of the change is important for the gently changing signal [9].

The dwt2 command provided in the Matlab wavelet toolbox performs single-level, two-dimensional wavelet decomposition for specific wavelets or specific wavelet decomposition filters (Lo_D and Hi_D).

[cA,cH,cV,cD] = dwt2 (X, “wname”) contains the wavelet name in the input matrix X and the string “wname”.

[cA,cH,cV,cD] = dwt2 (X,Lo_D,Hi_D) calculates the two-dimensional wavelet decomposition based on the specified wavelet decomposition filter, as shown above. Here, Lo_D is a decomposition low-pass filter, and Hi_D is a decomposition high-pass filter, and the two are equal in length. Figure 3 shows an example of the wavelet transformation of the input images.

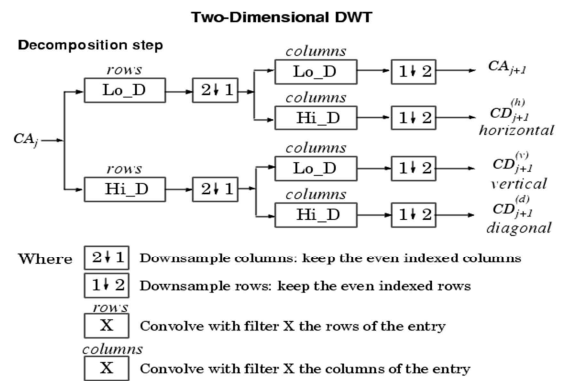


Figure 3. An illustration of 2D DWT

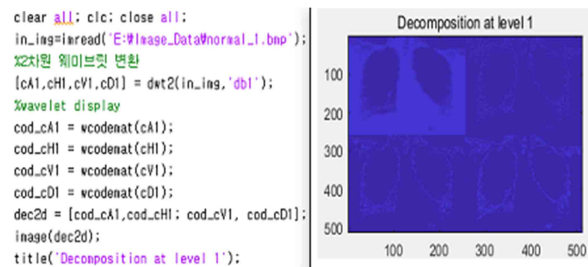


Figure 4. An example of wavelet decomposition

III. Experiment and Results

The final goals of this study were to standardize aspects, to extract features by DWT using the COVID-19 dataset, and to establish a system for automatic determination of the presence or absence of COVID-19 lung disease through mechanical learning combined with clinical data.

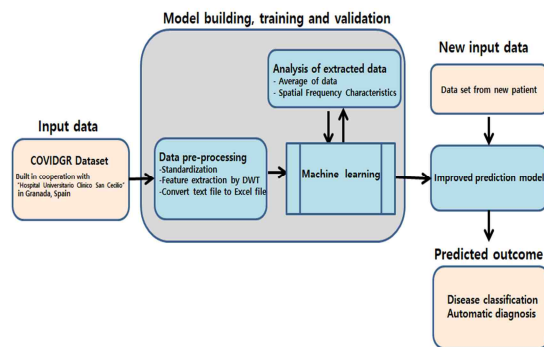


Figure 5. The research concept and final goal

In this paper, we extracted the features shown in Figure 6, stored them as a COVID-19 feature dataset, and analyzed their spatial frequencies.

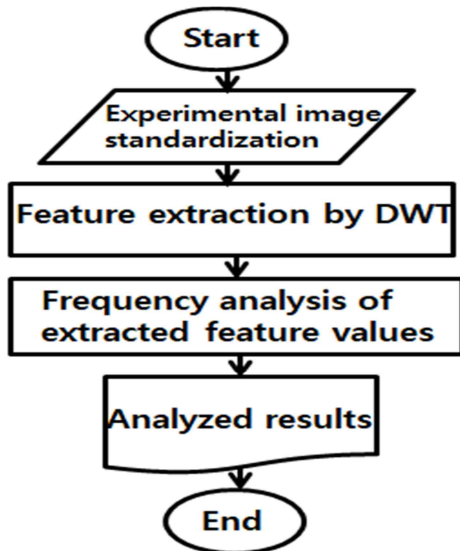


Figure 6. A flowchart of the feature extraction and spatial frequency analysis process

1. Image standardization

The COVIDGR Dataset was assembled in

collaboration with the Hospital Universitario San Cecilio in Granada, Spain, from the homogeneous and balanced COVIDGR-1.0 Database, which includes images of patients confirmed by RT-PCR as COVID-19-positive and ranked in severity as mild, moderate, or severe. However, many images obtained early in the COVID-19 pandemic were derived from basic CXRs. Therefore, the images in the COVIDGR Dataset were standardized according to the basics of chest imaging. Figure 7 shows examples of original and standardized images.

	Original Image	Standardization Image
Normal Image		
Mild Image		
Moderate Image		
Severe Image		

Figure 7. Examples of standardization images

2. Feature extraction

The standardized images were extracted by DWT, and the average feature values obtained by disease severity by summing the feature values of the extracted images are shown in Tables 1 through 4.

Table 1. Feature extraction values of normal images

Approximation	-0.10938	-0.07842	-0.05678	-0.03612	-0.02478	-0.01041	0.007	0.023381	0.028853	0.037144	0.049475	0.058997	0.072559	0.085281	0.097234	0.109373
Horizontal	-0.1028	-0.10452	-0.10561	-0.10687	-0.1075	-0.1083	-0.10927	-0.11019	-0.11048	-0.11084	-0.11157	-0.11216	-0.11291	-0.11362	-0.11428	-0.11496
Vertical	-0.10162	-0.10134	-0.10115	-0.10095	-0.10065	-0.10071	-0.10055	-0.1004	-0.10035	-0.10028	-0.10017	-0.10007	-0.09995	-0.09984	-0.09973	-0.09962
Diagonal	1.25E-06	6.25E-07	-1.0E-06	-1.3E-06	-1.9E-06	-1.9E-06	-1.3E-06	-1.3E-06	-6.3E-07	-1.3E-06	-1.3E-06	-1.3E-06	-2.5E-06	-2.5E-06	-1.3E-06	-1.3E-06

Table 2. Feature extraction values of mild images

Approximation	-0.05	-0.03585	-0.02687	-0.01651	-0.01133	-0.00478	0.0032	0.01078	0.01319	0.01698	0.02216	0.02697	0.03317	0.03889	0.04445	0.05
Horizontal	-0.04679	-0.04696	-0.04907	-0.04919	-0.04926	-0.04934	-0.04943	-0.04952	-0.04955	-0.0496	-0.04966	-0.04972	-0.0498	-0.04987	-0.04993	-0.05
Vertical	-0.04957	-0.04958	-0.04958	-0.04959	-0.0496	-0.0496	-0.04961	-0.04961	-0.04961	-0.04962	-0.04962	-0.04962	-0.04963	-0.04963	-0.04964	-0.04964
Diagonal	0	-0.00001	-0.00001	-0.00001	-0.00001	-0.00001	-0.00001	-0.00001	-0.00001	-0.00001	-0.00002	-0.00002	-0.00002	-0.00002	-0.00002	-0.00002

Table 3. Feature extraction values of moderate images

Approximation	-0.5	-0.5385	-0.2887	-0.1651	-0.1133	-0.0476	0.032	0.1078	0.1319	0.1698	0.2216	0.2897	0.3317	0.3899	0.4445	0.5
Horizontal	-0.45801	-0.45749	-0.4571	-0.45671	-0.45625	-0.45593	-0.45564	-0.45535	-0.45541	-0.4552	-0.45502	-0.45478	-0.45455	-0.45434	-0.45412	
Vertical	-0.45023	-0.44893	-0.44811	-0.44718	-0.44609	-0.44536	-0.44467	-0.44444	-0.4441	-0.44362	-0.44318	-0.44263	-0.44209	-0.44158	-0.44108	
Diagonal	0.00001	0.00001	0.00001	0.00001	0	0.00001	0.00001	0.00001	0.00001	0.00002	0.00002	0.00002	0.00002	0.00002	0.00002	0.00002

Table 4. Feature extraction values of severe images

Approximation	-0.4	-0.2868	-0.21496	-0.13208	-0.09064	-0.03808	0.0256	0.08624	0.10552	0.13584	0.17728	0.21576	0.26536	0.31192	0.3556	0.4
Horizontal	-0.39633	-0.40273	-0.40677	-0.41145	-0.4138	-0.41677	-0.42037	-0.4238	-0.42486	-0.42658	-0.42893	-0.43109	-0.4339	-0.43653	-0.43899	-0.4415
Vertical	-0.39422	-0.3946	-0.39484	-0.39512	-0.39542	-0.39563	-0.39584	-0.39591	-0.396	-0.39614	-0.39626	-0.39641	-0.39658	-0.39674	-0.39687	
Diagonal	0.00002	0.00002	0.00002	0.00004	0.00005	0.00005	0.00007	0.00008	0.00007	0.00009	0.00009	0.00009	0.00009	0.0001	0.0001	0.00012

3. Spatial frequency analysis

The average feature values extracted by disease were analyzed to determine the Approximation, Horizontal, Vertical, and Diagonal frequency characteristics. Figure 8 shows the low-frequency region of Approximation by disease severity. Normal images cover a large area; the mild and moderate images are similar, and the severe images do not appear at all.

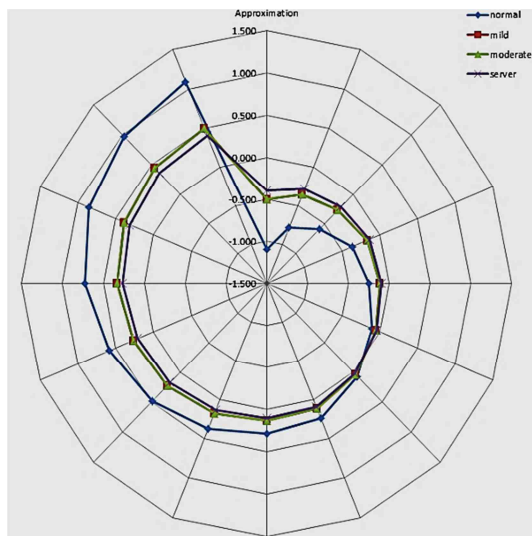


Figure 8. Spatial frequency analysis of the approximation data

Figure 9 shows the Horizontal section by disease. The normal images cover a large area. The mild and moderate images are similar, and the severe images

represent very small areas.

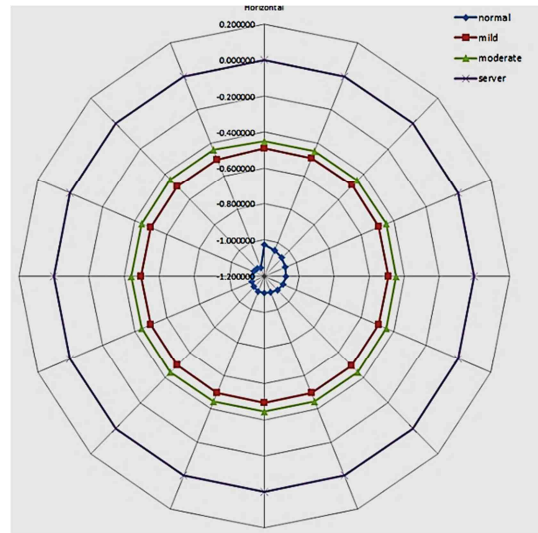


Figure 9. Spatial frequency analysis of the Horizontal data

Figure 10 shows the Vertical section by disease severity. The normal images and the mild and moderate severity images are similar, and severe images represent very small areas.

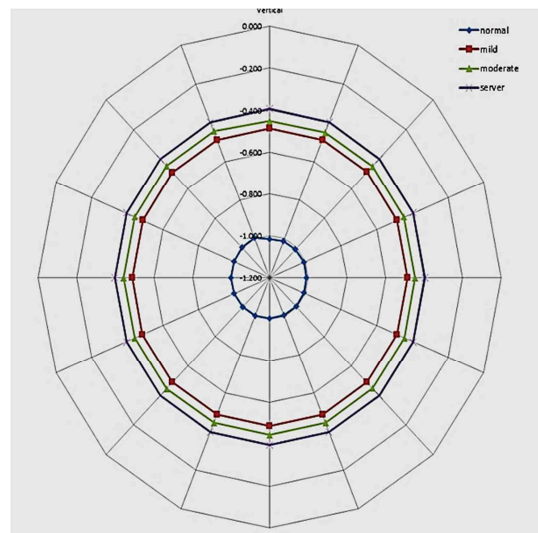


Figure 10. Spatial frequency analysis of Vertical data

Figure 11 shows the Diagonal characteristics by disease severity. The severe images represent a wide range, while the normal and moderate images are

similar. The mild images represent small areas and are skewed to one side.

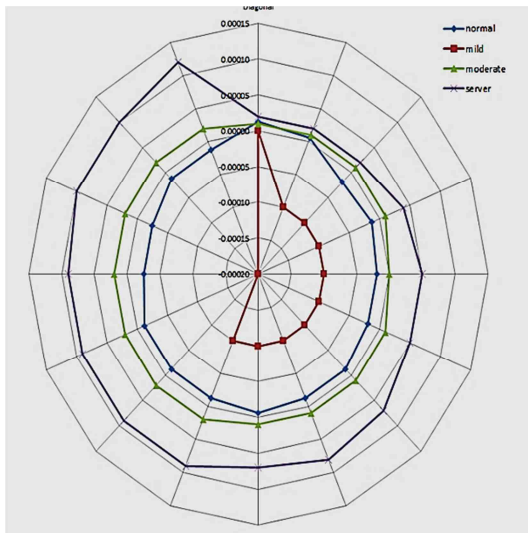


Figure 11. Spatial frequency analysis of the Diagonal data

IV. Discussion

Since the COVIDGR Dataset was obtained in urgent situations, there was a departure from the basic methods of breast imaging. Therefore, the images in the COVIDGR Dataset have been standardized to adhere to the basic methods of chest imaging (Figure 7). The standardized pixel format included 512 x 512 images and was intended to include all lung fields, except that the original image did not include the lung apex part. The standardized images were saved by DWT as the characteristics of Approximation, Horizontal, Vertical, and Diagonal are extracted and COVIDGR-19 Feature Data^{[10][11]}. The COVIDGR-19 Feature Data were entered into an Excel file to calculate the sum, and the average value was obtained and confirmed as the “Feature value of images by disease.”^{[11][12]} A frequency (Approximation, Horizontal, Vertical, Diagonal) analysis was performed [10].

Approximation analysis revealed that normal images

occupy a large area; mild and moderate images are similar, and severe images are not shown at all. Severe images are likely due to severe pneumonia, and most of the characteristic values are high-frequency (video-changing) components.

The Horizontal images have a large area. The mild and moderate images are similar, and the severe images represent very small areas, resulting in similar results to the Approximation analysis.

The Vertical images had similar results as the normal images, and the mild and moderate images represented very small areas.

The Diagonal shows a wide range of severe images. The normal and moderate images are similar, while the mild images represent a small area, and the image appears to be skewed to one side.

V. Conclusion

In this study, the CXR images in the COVIDGR Dataset were formatted, and the features of the normal images and disease images (mild, moderate, and severe) were extracted by DWT in an approximation, horizontal, vertical high frequency region (Vertical) and a diagonal post-frequency region (Diagonal).

The standardized format used 512 x 512 images and was intended to include all lung fields, except that the original image did not include the apex of the lung. The standardized images were extracted by DWT for the characteristics of Approximation, Horizontal, Vertical, and Diagonal and were stored as COVIDGR-19 feature data. The COVIDGR-19 feature data were entered into an Excel file to calculate the sums, and the average values were obtained and confirmed as the “Feature value of images by disease.”

A frequency (Approximation, Horizontal, Vertical, and Diagonal) analysis of feature extraction values by disease severity produced the following results.

Approximate: Normal images occupy a large area. Mild and moderate images are similar, and severe images are not present.

Horizontal: Regular images cover large areas. Mild images and moderate images are similar, and severe images are very small.

Vertical: Normal images and mild and moderate images are similar, while the severe images occupy very small areas.

Diagonal: The severe images were broad in scope. The normal images and the moderate images were similar, and the mild images showed a small, one-sided area.

Studies have shown that severe images have little or no approximation, a high diagonal content, and similar horizontal and vertical values. Normal images traditionally have the largest proportion of approximation because there is little change in frequency due to the absence of disease. The mild images and moderate images were similar in approximation, horizontal, and vertical but produced a one-sided bias in small areas in diagonal.

The results of this study can be used for development of an automatic identification system of CXR images.

[References]

[1] Jung Yeon Heo, “Clinical and Epidemiology Characteristics of Coronavirus Disease 2019 in the Early Stage of Outbreak”, Korean J Med. (2020) Vol. 95, No. 2, PP. 67-73

[2] Cristina Mesa Vieira, Oscar H. Franco, Carlos Gómez Restrepo, et. Al. “COVID-19: The forgotten priorities of the pandemic”, Maturitas, Vol. 136, June (2020), pp. 38-41.

[3] Coleen A. Boyle, Michael H. ScD, Susan M. Naverkamp, Jennifer Zubler, “The public health

response to the COVID-19 pandemic for people with disabilities”, Disability and Health Journal, Vol. 13, Issue 3, July(2020), 100943.

[4] Marco Ciotti, Massimo Ciccozzi, Alessandro Terrinoni, et. al., “The COVID-19 pandemic”, Critical Reviews in Clinical Laboratory Sciences, Vol. 57, Special issue:COVID-19 Pandemic and the Critical Role of the Clinical Laboratory, PP. 365-388

[5] Ki-il Lee, Dong Kyu Kim, Ju-Hun Mo, “Clinical Reviews of COVID-19 for Otorhinolaryngologists”, J Rhinol, (2021)Vol. 28, No. 1, PP. 1-13

[6] So-Hee Hong, Hyo-Jung Park, Jae-Hwan Nam, “Lessons Learned from SARS-CoV: Preparation for SARS-CoV-2 induced COVID-19”, The Korean Society for Microbiology, (2020) Vol. 50, No. 2, pp. 76-96

[7] S. Tabik, A. Gomez-Rios, J. L. Martin-Rodriguez, et al, “COVIDGR Dataset and COVID-SDNet Methodology for Predicting COVID-19 Based on Chest X-Ray Images”, IEEE Journal of Biomedical and Health Informatics, (2020), Vol. 24, Issue 12, PP. 3595-3605

[8] Christopher Torrence, Gilbert P. Compo, “A Practical Guide to Wavelet Analysis”, Bulletin of the American Meteorological Society, Vol. 79, Issue 1(1998), PP. 61-78.

[9] E. P. Serrano, M.A. Fabio, “Application of the wavelet transform to acoustic emission signals processing”, IEEE Transactions on Signal Processing, Vol. 44, Issue 5(1996), pp. 1270-1275.

[10] Sang-bock Lee, Hwunjae Lee, V. R. Singh, “Determining the Degree of Malignancy on Digital Mammograms by Artificial Intelligence Deep Learning”, j Med Imaging(ScholarGen)(2020), Vol. 03, No. 1, PP. 17-32

[11] Junhaeng Lee, “Analysis of the DWT Characteristics of MR Molecular Images Obtained by Using MNPCA”, j Med Imaging(ScholarGen), Vol. 01, No. 01(2018), PP. 1-15.

[12] R. Vijayarajan, S. Muttan, : Discrete wavelet transform based principal component averaging fusion for medical images”, AEU-International Journal of Electronics and Communications, Vol. 69, Issue 6, June(2015), PP. 896-902.

Evaluation of Brain Glioblastoma Images Using Podoplanin-targeted Manganese Ferrite in 9.4T MRI

Seung-Hyun Yang,¹ Yong-Min Huh,^{2,*} Hwunjae Lee^{1,2,3*}

Received : 5 July 2021 / Accepted : 2 November 2021 / Published online 28 December 2021

©The Author(s) 2021

©The Author(s) 2021

Abstract To detect brain glioblastoma, which is difficult to treat and has a very poor prognosis, a method for early detection on magnetic resonance imaging (MRI) using podoplanin (PDPN), a biomarker for glioblastoma, is proposed in the present study. Magnetic nanoparticle (MNP)-PDPN was prepared using manganese (Mn) iron targeting PDPN. Axial and coronal images of 3 brain model (GSC11_G19_No.4) mice were acquired with a 9.4T high-magnetic field MRI, and an experiment was conducted. The mean value and standard deviation were larger in the image after the contrast agent (MNP-PDPN) was injected, confirming that injection of the contrast agent improved the image of the brain glioblastoma area. In addition, the area of the segmented image using the region of interest was large in the image obtained after injection of contrast agent (MNP-PDPN). PSNR evaluation showed values from 13.77 dB–20.09 dB. In conclusion, in the present study, the MNP-PDPN contrast agent was shown useful for early detection of brain glioblastoma. Future research is needed to develop a theragnostic technology to diagnose and treat glioblastoma simultaneously using MNP-PDPN.

Key words: Glioblastoma, Early detection, Contrast agent, MRI evaluation, PSNR

I. Introduction

Modern medicine is based on understanding human health and controlling the course of chronic diseases, correcting disabling physical conditions, and treating molecular deficiencies [1]. The expected medicine of the future will detect diseases at an early stage and develop into personalized and precision medicine based on individual diseases [2]. A brain tumor is a mass of cells that grow abnormally, and various types exist. Brain tumors can be benign or malignant, as well as primary or metastatic. Growth speed of a brain tumor varies greatly depending on the type of brain tumor, and the location and growth rate of the brain tumor have a significant effect on the nervous system. Among brain tumors, glioblastoma multiforme is a deadly intracranial cancer with an aggressive malignant progression. This tumor is highly resistant to conventional combination therapies such as traditional radiation and chemotherapeutic agents [3]. Therefore, early detection of glioblastoma is very important for effective treatment. Traditionally, magnetic

Seung-Hyun Yang,¹ Yong-Min Huh,²
Hwunjae Lee^{1,2,3*} Corresponding author (✉)

¹ Department of Radiology, College of Medicine, Yonsei University, Seoul 03722, Republic of Korea

² YUHS-KRIBB Medical Convergence Research Institute, Yonsei University Health System, Seoul 03722, Republic of Korea

³ Graduate Program of Nanoscience and Technology, College of Medicine, Yonsei University, Seoul 03722, Republic of Korea

resonance imaging (MRI) plays an important role in the imaging of angiogenesis in the tumor microenvironment and is important for predicting cancer metastasis [4]. However, MRI has low sensitivity. The use of optical imaging can increase sensitivity and compensate for the MRI shortcomings [5]. In particular, optical imaging can increase the contrast and sensitivity to new blood vessels, creating a synergistic effect. In the present manuscript, a technique is proposed for early detection of glioblastoma on MRI using podoplanin (PDPN) as a biomarker to detect glioblastoma, which is difficult to treat and has a very poor prognosis. Therefore, magnetic nanoparticle (MNP)-PDPN contrast agent was developed using manganese (Mn) iron targeting PDPN. For the experiment, images of 9 mouse brains (GSC11_G19_No.4) were acquired with a 9.4T high-magnetic field MRI device. The image processing results confirmed good resolution using the MNP-PDPN contrast agent. Future research goals include synthesizing the therapeutic agent in MNP-PDPN contrast agent to develop theragnostic technology targeting glioblastoma cells.

II. Materials and methods

1. *Animal model and experimental procedure*

All animal experiments were conducted with the approval of the Association for Assessment and Accreditation of Laboratory Animal Care International. Female BALB/C-Slc nude mice 7–8 weeks of age were anesthetized by intraperitoneal injection of Zoletil/Rompun mixture, and 200 mL of saline containing 1.0×10^7 GSC11 cells was injected into the brain. After cancer cell implantation, MRI was performed at 2–3 weeks. Glioblastoma multiforme is a lethal intracranial cancer that exhibits

an aggressive malignant progression highly resistant to conventional combination therapies such as radiation and chemotherapy agents [3]. Therefore, early detection of glioblastoma is critical for effective treatment. Traditionally, because MRI plays a major role in the imaging of neovascularization in the tumor microenvironment, predicting the metastasis of cancer is very important [4]. However, MRI has low sensitivity, and use of optical imaging enables an increase in sensitivity and compensates for the disadvantages of MRI [5]. In particular, optical imaging can increase the contrast and sensitivity for new blood vessels, which can result in great synergy.

2. *Glioblastoma biomarkers*

Podoplanin (PDPN) is a transmembrane mucin-like protein broadly associated with lymphatic endothelium and lymphangiogenesis, and it augments the separation of blood and lymphatic vessels during embryonic development. Widespread PDPN expression has been described in various human tumors in which platelet aggregation caused by PDPN through C-type lectin-like receptor-2 (CLEC-2) has been associated with metastasis [6]. In addition, PDPN has been linked to cytoskeleton regulation and increased migration and invasion. In gliomas, a grade-dependent expression of PDPN usually is found in tumor cells.

3. *Magnetic nanoparticles*

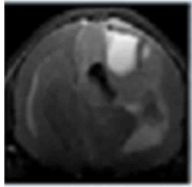
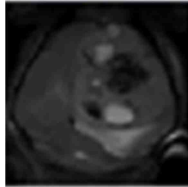
Manganese ferrite has become an important research area in the past two decades mainly due to its magneto-optical and magneto-resistive properties, which are applied in various fields from technology to medicine [7, 8]. Ferrites are usually metal oxides with iron as the main metallic constituent. These ferrites have a superparamagnetic property that

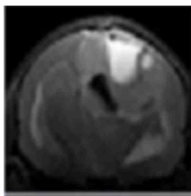
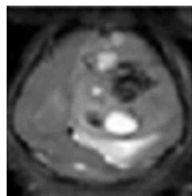
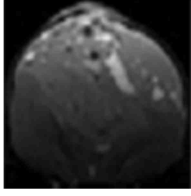
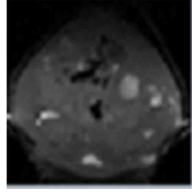
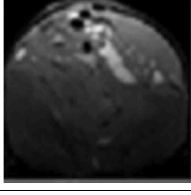
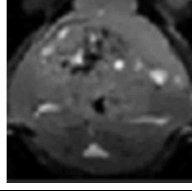
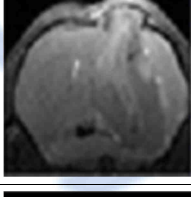

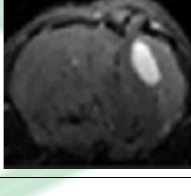

allows wide use in the field of biomedical applications [9]. However, as most are susceptible to weak chemical stability, surface modification or doping of other elements is necessary. Therefore, researchers use doping elements such as Co, Mg, Mn, Zn, and Ni to produce chemically stable ferrites in biological systems and for tuning their magnetic behavior [10]. Among ferrites, Mn ferrite is a well-known soft magnetic material with high coercivity, moderate magnetization, excellent physiochemical stability, and high cubic magneto-crystalline anisotropy, for which it is used for various biological applications [11]. Mn-doped ferrite is an efficient MRI contrast agent compared with magnetite because it has the same saturation magnetization as iron oxide but possesses a higher order of crystalline anisotropy, causing slower magnetic moment relaxation [12]. Furthermore, anisotropic nanostructures have attracted much interest in recent years [13]. Therefore, various synthesis techniques have been developed to produce different nanostructure shapes such as rods, prisms, octahedrals, and cubes.

4. Image acquisition

All MRI experiments were performed using a 9.4T Bruker BioSpec scanner (RF SUC 400 1H M-BR-LIN ROAD, Bruker Medical Systems, Germany).

Table 1. Results of 9.4T MRI

	<i>Agent Inj.</i>	<i>T2 Axial Image</i>	<i>T2 Coronal Image</i>
<i>Model_1</i>	<i>Before inj.</i>		

	<i>After inj.</i>		
<i>Model_2</i>	<i>Before inj.</i>		
	<i>After inj.</i>		
<i>Model_3</i>	<i>Before inj.</i>		
	<i>After inj.</i>		

5. Image quality evaluation based on contrast agent injection

Image quality evaluation characterizes the content and texture of an image. Basically, evaluation metrics can be categorized into primary, secondary, and higher-order scales. Primary metrics focus on properties such as mean intensity, standard deviation, and variance. Therefore, first-order metrics only measure individual pixels in the image and do not account for spatial relationships between pixels, ignoring neighbor relationships. Conversely, quadratic or higher metrics measure the properties of two or more pixels relative to each other at a specific location. In medical images, the mean often is used

as a matrix representative value of pixels. The standard deviation of one of the scatter plots is representative of dispersion of the medical image pixel data around the mean. A standard deviation close to 0 indicates that the data values are concentrated near the mean, and a larger standard deviation indicates that the data values are spread more widely. Peak signal-to-noise ratio (PSNR) is the maximum signal-to-noise ratio, an objective measurement method that numerically indicates the difference between the image before contrast agent injection and the image after contrast agent injection during medical image evaluation. PSNR is most easily defined as the mean square error (MSE). Given a before contrast agent injection image $m \times n$ monochrome image I and an after contrast agent injection image approximation K , MSE is defined as:

$$MSE = \frac{1}{m \cdot n} \sum_{i=0}^{m-1} \sum_{j=0}^{n-1} [I(i, j) - K(i, j)]^2 \quad (1)$$

The PSNR (in dB) is defined as:

$$\begin{aligned} PSNR &= 10 \cdot \log_{10} \left(\frac{MAX_I^2}{MSE} \right) \\ &= 20 \cdot \log_{10} \left(\frac{MAX_I}{\sqrt{MSE}} \right) \\ &= 20 \cdot \log_{10}(MAX_I) - 10 \cdot \log_{10}(MSE) \end{aligned} \quad (2)$$

Here, MAX_I is the maximum possible pixel value of the image. When the pixels are represented using 8 bits per sample, MAX_I is 255. More generally, when samples are represented using linear pulse-code modulation (PCM) with B bits per sample, MAX_I is $2^B - 1$. Image processing for image evaluation was performed with an M-program using MATLAB image processing toolbox as shown in Figure 1.

```
ROI_segmentation.m x Untitled x +
- thresholdValue = 127;
- binaryImage = originalImage > thresholdValue; % Bright objects will be chosen if you use >.
- % ===== IMPORTANT OPTION =====
- % Use < if you want to find dark objects instead of bright objects.
- % binaryImage = originalImage < thresholdValue; % Dark objects will be chosen if you use <.
- % Do a "hole fill" to get rid of any background pixels or "holes" inside the blobs.
- binaryImage = imfill(binaryImage, 'holes');
- % Show the threshold as a vertical red bar on the histogram.
- hold on;
- maxYValue = ylim;
- line([thresholdValue, thresholdValue], maxYValue, 'Color', 'r');
- % Place a text label on the bar chart showing the threshold.
- annotationText = sprintf('Thresholded at %d gray levels', thresholdValue);
- % For text(), the x and y need to be of the data class "double" so let's cast both to double.
- text(double(thresholdValue + 5), double(0.5 + maxYValue(2)), annotationText, 'FontSize', 10, 'Color', [0 .5 0]);
- text(double(thresholdValue - 70), double(0.94 + maxYValue(2)), 'Background', 'FontSize', 10, 'Color', [0 0 .5]);
- text(double(thresholdValue + 50), double(0.94 + maxYValue(2)), 'Foreground', 'FontSize', 10, 'Color', [0 0 .5]);
- % Display the binary image.
- subplot(3, 3, 3);
- imshow(binaryImage);
- title('Binary Image, obtained by thresholding', 'FontSize', captionFontSize);
```

Figure 1. MATLAB program for the experiment

III. Experiment and Results

1. Experimental process

All MRI experiments were performed using a 9.4T Bruker BioSpec scanner (RF SUC 400 1H M-BR-LIN ROAD, Bruker Medical Systems). The following parameters were used at room temperature for T2 and FLASH sequences: T2 sequence (Echo = 1, TR = 2300 ms, TE = 22.0 ms, FA = 180 deg, TA = 0 h 4 m 54 s 400 ms, NEX = 2, FOV = 4.00); FLASH sequence (TR: 280.0 ms, FA = 25 deg, TA = 0 h 7 m 10 s, NEX = 4, FOV = 4.00). The experiment was evaluated by comparing the images before and after injection of contrast agent in the order shown in Figure 2.

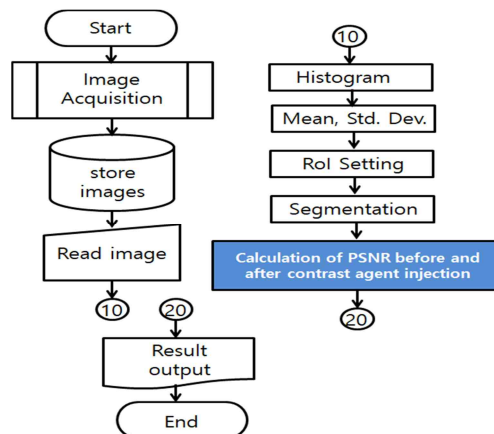


Figure 2. Experiment flow chart

2. Experimental results

To evaluate the 9.4T MRI images of brain glioblastoma before and after contrast agent injection, the acquired images were pre-processed with 256×256 -pixel 256-level grayscale images. The mean value and standard deviation of each pixel of the pre-processed original image were calculated. Then, the distribution of pixels was confirmed on a histogram of the image, and the image was segmented after setting the region of interest. Tables 2–7 show the experimental results of T2 axial and T2 coronal images before and after contrast agent injection in experimental Models 1–3.

Table 2. T2 Axial experimental results of Model 1

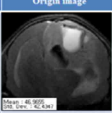
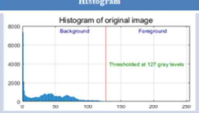

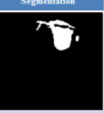
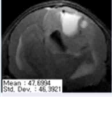
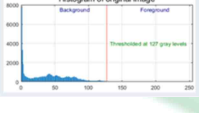
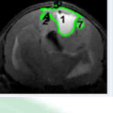

	Origin image	Histogram	RoI(Region of Interest)	Segmentation
No injection	 Mean: 46.922 Std. Dev.: 20.265	 Histogram of original image Background Foreground Thresholded at 127 gray levels		
Injection	 Mean: 41.624 Std. Dev.: 20.202	 Histogram of original image Background Foreground Thresholded at 127 gray levels		

Table 3. T2_Coronal experimental results of Model 1



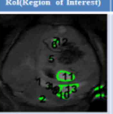
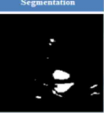
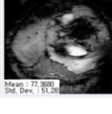
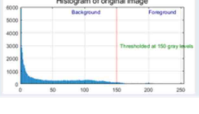
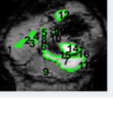

	Origin image	Histogram	RoI(Region of Interest)	Segmentation
No injection	 Mean: 37.111 Std. Dev.: 23.342	 Histogram of original image Background Foreground Thresholded at 100 gray levels		
Injection	 Mean: 37.399 Std. Dev.: 17.101	 Histogram of original image Background Foreground Thresholded at 100 gray levels		

Table 4. T2 Axial experimental results of Model 2

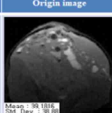

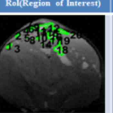

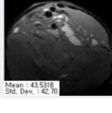
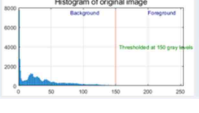
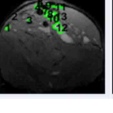
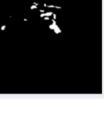
	Origin image	Histogram	RoI(Region of Interest)	Segmentation
No injection	 Mean: 38.111 Std. Dev.: 18.111	 Histogram of original image Background Foreground Thresholded at 100 gray levels		
Injection	 Mean: 41.322 Std. Dev.: 42.111	 Histogram of original image Background Foreground Thresholded at 100 gray levels		

Table 5. T2_Coronal experimental results of Model 2

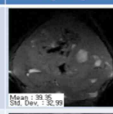
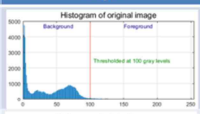
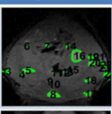
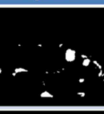
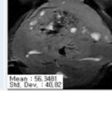
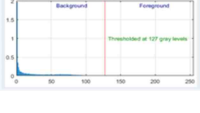
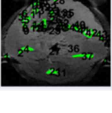

	Origin image	Histogram	RoI(Region of Interest)	Segmentation
No injection	 Mean: 38.111 Std. Dev.: 18.111	 Histogram of original image Background Foreground Thresholded at 100 gray levels		
Injection	 Mean: 56.222 Std. Dev.: 42.111	 Histogram of original image Background Foreground Thresholded at 100 gray levels		

Table 6. T2 Axial experimental results of Model 3

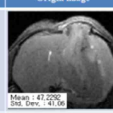
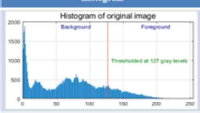
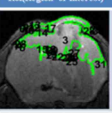

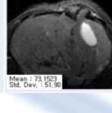
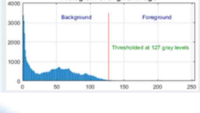
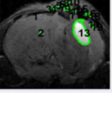

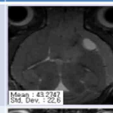
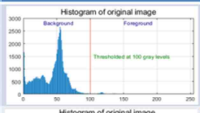
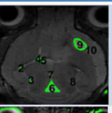

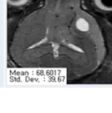
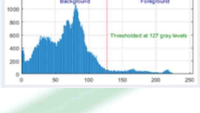
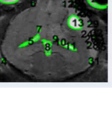

	Origin image	Histogram	RoI(Region of Interest)	Segmentation
No injection	 Mean: 43.222 Std. Dev.: 20.265	 Histogram of original image Background Foreground Thresholded at 127 gray levels		
Injection	 Mean: 71.111 Std. Dev.: 42.111	 Histogram of original image Background Foreground Thresholded at 127 gray levels		

Table 7. T2_Coronal experimental results of Model 3

	Origin image	Histogram	RoI(Region of Interest)	Segmentation
No injection	 Mean: 41.222 Std. Dev.: 20.265	 Histogram of original image Background Foreground Thresholded at 100 gray levels		
Injection	 Mean: 68.667 Std. Dev.: 36.67	 Histogram of original image Background Foreground Thresholded at 127 gray levels		

The experimental results showed larger mean and standard deviation in the image after contrast agent injection than in the image before injection. In the histogram, the background showed a much larger distribution of pixels, and the foreground area (with glioblastoma) showed a small value. When the image was segmented with the region of interest as the boundary of the threshold value, the image after contrast agent injection showed a larger segmented region than did the image before injection.

Table 8 shows the MSE and PSNR calculations for T2 sequence axial images before and after contrast agent injection for experimental Model 1. In the experiment, MSE was 636, root mean square error (RMSE) was 25.22, and PSNR was 20.09 dB.

Table 8. T2 axial images of experimental Model 1

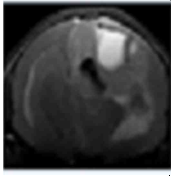
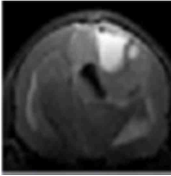
<i>Pre-injection</i>	<i>Post-injection</i>	<i>Result</i>	
		MSE	636.2
		RMSE	25.22
		PSNR	20.09

Table 9 shows the MSE and PSNR calculations for T2 sequence coronal images before and after contrast agent injection in experimental Model 1. In the experiment, MSE was 2,727, RMSE was 52.22, and PSNR was 13.77 dB.

Table 9. T2 coronal images of experimental Model 1

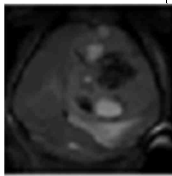
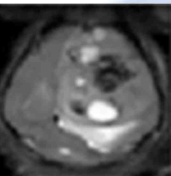
<i>Pre-injection</i>	<i>Post-injection</i>	<i>Result</i>	
		MSE	2,727
		RMSE	52.22
		PSNR	13.77

Table 10 shows the MSE and PSNR calculations for T2 sequence axial images before and after contrast agent injection in experimental Model 2. In the experiment, MSE was 699.90, RMSE was 26.46, and PSNR was 19.68 dB.

Table 10. T2 axial images of experimental Model 2

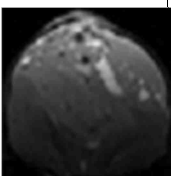
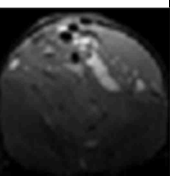
<i>Pre-injection</i>	<i>Post-injection</i>	<i>Result</i>	
		MSE	699.89
		RMSE	26.455
		PSNR	19.680

Table 11 shows the MSE and PSNR calculations for T2 sequence coronal images before and after contrast agent injection in experimental Model 2. In the experiment, MSE was 1,570, RMSE was 39.62, and PSNR was 16.70 dB.

Table 11. T2 coronal images of experimental Model 2

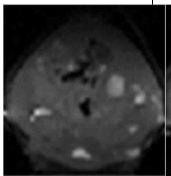
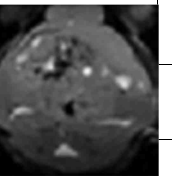
<i>Pre-injection</i>	<i>Post-injection</i>	<i>Result</i>	
		MSE	1,570.33
		RMSE	39.6274
		PSNR	16.1709

Table 12 shows the MSE and PSNR calculations for T2 sequence axial images before and after contrast agent injection in experimental Model 3. In the experiment, MSE was 2,006, RMSE was 44.78, and PSNR was 15.11 dB.

Table 12. T2 axial images of experimental Model 3

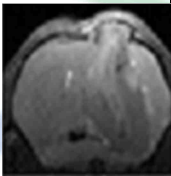
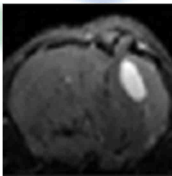
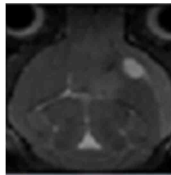
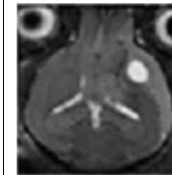
<i>Pre-injection</i>	<i>Post-injection</i>	<i>Result</i>	
		MSE	2,005.9
		RMSE	44.78
		PSNR	15.10

Table 13 shows the MSE and PSNR calculations for T2 sequence coronal images before and after contrast agent injection in experimental Model 3. In the experiment, MSE was 1,983, RMSE was 44.53, and PSNR was 15.16 dB.

Table 13. T2 coronal images of experimental Model 3

<i>Pre-injection</i>	<i>Post-injection</i>	<i>Result</i>	
		MSE	1,983
		RMSE	44.53
		PSNR	15.15

IV. Discussion

and after contrast agent injection

Improving medical imaging or visual quality of digital images can be subjective, and it is uncertain whether one method produces a better-quality image. Therefore, establishing quantitative/empirical measures to compare the effect of image enhancement on image quality is necessary [14]. Quality analysis of medical images characterizes the content and texture of the image. Basically, rating scales can be classified into primary (first-order), secondary (second-order), and higher-order scales. Primary metrics focus on properties such as mean intensity, standard deviation, and variance and only measure individual pixels in the image. A first-order metric does not account for spatial relationships between pixels, leaving out neighbor relationships. A quadratic or higher metric measures the properties of two or more pixels relative to each other at a specific location. MSE is used to measure the difference between an expected outcome and the actual outcome. This metric is a variance measure and can be used to analyze image enhancements such as noise and blur removal [14]. The PSNR is an important metric used to measure the quality of the image when enhanced by a contrast agent. Higher PSNR value indicates higher quality rate. The MSE determines the PSNR value. When comparing two images, PSNR is calculated as the MSE between the pixel intensities and taking the ratio of the maximum possible intensity to the result of the calculation. The standard value of PSNR is 35–40 dB. In general, a higher PSNR value corresponds to a better-quality image. The PSNR standard value is subjected to correlation analysis and depends on MSE, which is indirectly proportional to the PSNR. The histogram represents the frequency of differences in intensity between two images [14].

1. Mean and standard deviation before

Average intensity plays a role in image contrast; the higher is the value, the greater is the contrast in the image. The average value represents the contribution of individual pixel intensities to the overall image. The standard deviation quantifies the amount of change in the image. This is an optimal metric for evaluating the quality of enhanced images and can be used in applications where images are enhanced by injecting a contrast agent. Table 8 shows the pixel mean values and standard deviations of the axial and coronal plane images before and after injection of contrast agent in experimental Models 1–3; the mean value and the standard deviation are larger in the image after contrast agent injection.

Table 14. Mean and standard deviation

Experimental Model	Contrast agent Injection	Axial		Coronal	
		Mean	Std. Dev.	Mean	Std. Dev.
1.	No Injection	46.96	42.43	35.25	25.67
	Injection	47.7	46.39	77.37	51.28
2.	No Injection	39.18	38.88	39.35	32.99
	Injection	43.53	42.7	56.35	40.82
3.	No Injection	47.23	41.06	43.27	22.6
	Injection	73.15	51.9	68.6	39.67

Figures 3 and 4 are graphs showing the contents of Table 14; the images after injection of the contrast agent in experimental Models 1–3 show larger values.

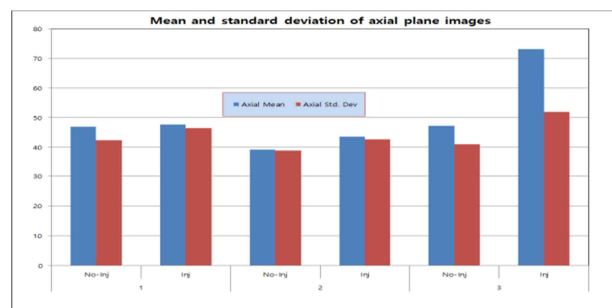


Figure 3. Mean and standard deviation of axial plane images

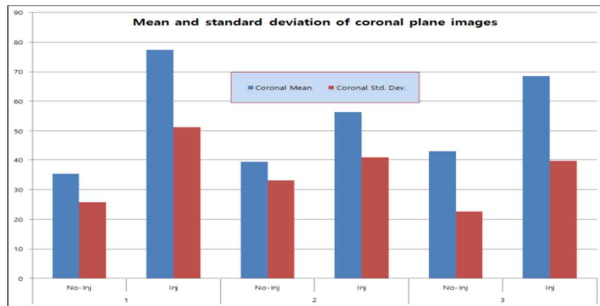


Figure 4. Mean and standard deviation of coronal plane images

2. PSNR evaluation before and after contrast agent injection

Higher PSNR value indicates higher quality rate. The MSE determines the PSNR value. When comparing two images, PSNR is calculated using the MSE between the pixel intensities and the ratio of the maximum possible intensity to the result of the calculation. In general, a higher PSNR value corresponds to a higher-quality image. The PSNR standard value is subjected to correlation analysis and depends on MSE, which is indirectly proportional to the PSNR.

Table 15. MSE, RMSE, and PSNR values

Model	Plane	MSE	RMSE	PSNR (dB)
Model_1	Axial	636.25	25.22	20.09
	Coronal	2,727	52.22	13.77
Model_2	Axial	699.9	26.46	19.68
	Coronal	1,570	39.63	16.17
Model_3	Axial	2,005	44.79	15.11
	Coronal	1,983	44.53	15.16

V. Conclusion

Herein, a method was proposed for early detection of glioblastoma based on MRI using PDPN as a biomarker to detect glioblastoma, which is difficult

to treat and has a very poor prognosis. The mean value, standard deviation, histogram, image segmentation, and PSNR of images acquired before and after contrast agent injection using the 9.4T MRI device were evaluated. Consequently, the following conclusions were obtained.

1. The mean value and standard deviation showed larger values in the image after contrast agent (MNP-PDPN) was injected, confirming that injection of the contrast agent enhanced the image of the brain glioblastoma area.
2. The area of the segmented image using the region of interest was large in the image obtained after injection of the contrast agent (MNP-PDPN), confirming that injection of the contrast agent enhanced the image of the brain glioblastoma area.
3. Based on PSNR evaluation, the values ranged from 13.77–20.09 dB.

In conclusion, in this study, the MNP-PDPN contrast agent was useful for early detection of brain glioblastoma. Future research to develop a theragnostic technology for simultaneous diagnosis and treatment of glioblastoma using MNPs-PDPN is needed.

[References]

- [1] Mbih Jerome Tosam, "The Role of Philosophy in Modern Medicine", Open Journal of Philosophy, Vol. 4, No. 1, PP. 75-84 (2014)
- [2] Rui Chen, Michael Snyder, "Promise of personalized omics to precision medicine", WIREs Mechanisms of Disease, Vol. 5, Issue 1, PP. 73-82.(2013)
- [3] R. Li, X. Chen, Y. You, X. Wang, Y. Liu, Q. Hu, W. Yan, "Comprehensive portrait of recurrent glioblastoma multiforme in molecular and clinical characteristics", Oncotarget. 6(31), 30968 (2015).
- [4] L. B. Nilsen, A. Fangberget, O. M. Geier, O.

- Engebraaten, E. Borgen, D. R. Olsen, T. Seierstad, "Associations Between Tumor Vascularization Assessed by In Vivo DCE-MRI and the Presence of Disseminated Tumor Cells in Bone Marrow in Breast Cancer Patients at the Time of Diagnosis", *J. Magn. Reson. Imaging* 40(6), 1382 (2014).
- [5] Y. Zhang, B. Zhang, F. Liu, J. Luo, J. Bai, "In vivo tomographic imaging with fluorescence and MRI using tumor-targeted dual-labeled nanoparticles", *Int. J. Nanomedicine* 9, 33 (2014).
- [6] Kato Y, Kaneko MK, Kunita A, Ito H, Kameyama A, Ogasawara S, Matsuura N, Hasegawa Y, Suzuki-Inoue K, Inoue O, Ozaki Y, Narimatsu H., "Molecular analysis of the pathophysiological binding of the platelet aggregation-inducing factor podoplanin to the C-type lectin-like receptor CLEC-2", *Cancer Sci.* 99, 54–61(2008)
- [7] Jinhao G, Hongwei G and Bing Xu, "Multifunctional Magnetic Nanoparticles: Design, Synthesis, and Biomedical Applications" *Accounts of Chemical Research*, 42(8) PP. 1097–107(2009)
- [8] Hazra S and Ghosh N N, "Preparation of nanoferrites and their applications", *J. Nanosci. Nanotechnol.*, 14(2), PP. 1983–2000(2014)
- [9] Ito A, Shinkai M, Honda H and Kobayashi, "Medical application of functionalized magnetic nanoparticles", *J. Biosci. Bioeng.* 100(1), PP. 1–11(2005)
- [10] Pu Y, Tao X, Zeng X, Le Y and Chen, "Synthesis of Co–Cu–Zn doped Fe₃O₄ nanoparticles with tunable morphology and magnetic properties", *J. Magn. Magn. Mater.*, 322(14) pp. 1985–1990(2010)
- [11] Lee J H, Jang J T, Choi J S, Moon S H, Noh S H, Kim J W et al., "Exchange-coupled magnetic nanoparticles for efficient heat induction", *Nat. Nanotechnol.* 6, pp. 418–22(2011)
- [12] Lu J, Ma S, Sun J, Xia C, Liu C, Wang Z et al., "Manganese ferrite nanoparticle micellar nanocomposites as MRI contrast agent for liver imaging", *Biomaterials*, 30(15), PP. 2919–28 (2009)
- [13] Baaziz W, Pichon B P, Liu Y, Grenèche J M, Ulhaq-Bouillet C, Terrier E et al., "Tuning of synthesis conditions by thermal decomposition toward core-shell Co_xFe_{1-x}O@Co_yFe_{3-y}O₄ and CoFe₂O₄ nanoparticles with spherical and cubic shapes", *Chem. Mater.*, 26(17), PP. 5063–5073(2014)
- [14] S. Rajkumar, G. Malathi, "A Comparative Analysis on Image Quality Assessment for Real Time Satellite Images", *Indian Journal of Science and Technology*, Vol. 9, No. 34, PP. 1-11(2016)

LOW-DOSE LIPOSOMAL AMPHOTERICIN B IN REFRACTORY INDIAN VISCERAL LEISHMANIASIS: A MULTICENTER STUDY

S. SUNDAR, T. K. JHA, C. P. THAKUR, M. MISHRA, V. P. SINGH, AND R. BUFFELS

Am. J. Trop. Med. Hyg., 66(2), 2002, pp. 143–146

Copyright 2002 by The American Society of Tropical Medicine and Hygiene

Abstract In this randomized, double-blind, dose-ranging, multicenter trial, 84 patients with visceral leishmaniasis refractory to antimony therapy were administered liposomal amphotericin B (AmBisome) at cumulative doses of 3.75, 7.5, and 15.0 mg/kg for 5 consecutive days. Posttreatment apparent cure and definite cure were assessed at 2 weeks and 6 months after the end of therapy, respectively. Mild to moderate infusion-related fever and rigors were seen in 29 and 44% of patients, respectively. One patient each in the 3.75- and 7.5-mg groups had detectable parasites on splenic smear at posttreatment evaluation. At 6 months' follow-up, however, 2, 1, and 1 patients relapsed in the 3.75-, 7.5-, and 15.0-mg groups, resulting in definite cure rates of 89, 93, and 97%, respectively. There was no significant difference in the cure rates of the 3 groups. Low-dose liposomal amphotericin B given for 5 days can cure most patients with Indian kala-azar

Key word : Refractory Indian Visceral Leishmaniasis; Low-dose liposomal amphotericin B; multicenter study

1. INTRODUCTION

Visceral leishmaniasis (VL), also known as kala-azar, affects a large population (12 million) in Bihar and neighboring states in India, with an estimated annual incidence of 100,000–250,000 cases.¹ If untreated, the disease is almost always fatal. Sodium stibogluconate (Sbv) is the first-line drug for its treatment. For the last 2 decades, there has been a steady decline in the response to Sbv; 37–64% of patients currently fail to be cured by antimony treatment.^{2–3} Alternative drugs are pentamidine and amphotericin B, but both are toxic. Declining efficacy of pentamidine⁴ leaves only amphotericin B for these Sbv-refractory patients. Administration of amphotericin B, which is given on alternate days for 1 month or more, is associated with infusion-related chills, rigors, and fever and with cardiac and renal toxicity.^{5,6} In order to alleviate the side effects, as well as to improve efficacy by targeted delivery, lipid-associated amphotericin B has been used in patients with refractory VL in India and elsewhere.^{7–14} The high cost of lipid formulations of amphotericin B puts them beyond the reach of most patients in developing countries. In this multicenter,

S. SUNDAR, T. K. JHA, C. P. THAKUR, M. MISHRA, V. P. SINGH, AND R. BUFFELS

Kala-azar Medical Research Center, Banaras Hindu University, Varanasi, India;

Kala-azar Research Center, Muzaffarpur, India; Balaji Uthan Sansthan, Patna, India;

Kala-azar Research Center, Darbhanga, India; Gilead Sciences, Paris, France

dose-ranging study, low-dose liposomal amphotericin B (AmBisome, Gilead Sciences, Inc., Foster City, CA) was used for 5 days in an effort to find an affordable and effective regimen for patients refractory to initial Sbv treatment. The aim of the trial was to determine the lowest dose of liposomal amphotericin B able to cure at least 90% of the patient population

2. PATIENTS AND METHODS

Eighty-four patients enrolled in this trial were randomized to receive the following regimens of liposomal amphotericin B infusions: 1) Group A, 0.75 mg/kg per day for 5 consecutive days (cumulative dose, 3.75 mg/kg); 2) Group B, 1.5 mg/kg per day for 5 consecutive days (cumulative dose, 7.5 mg/kg); and 3) Group C, 3.0 mg/kg per day for 5 consecutive days (cumulative dose, 15 mg/kg). Four centers participated, and recruitment of 21 patients (7 per group) at each center was planned. The ethical committees of the Institute of Medical Sciences, Banaras Hindu University; the Kala-azar Research Center, Muzaffarpur; Balaji Uthan Sansthan, Patna; and the Kala-azar Research Center, Darbhanga, approved the protocol, and the trial was conducted as per Good Clinical Practices (ICH E6) and the Declaration of Helsinki. Written informed consent from patients or legal guardians of minors were obtained before the inclusion in the trial, which included consent for the pre- and posttreatment splenic/bone marrow aspirates and testing for human immunodeficiency virus (HIV). Patients of any age or sex were eligible for enrollment into the trial if they had signs and symptoms of VL confirmed by the presence of parasites in splenic or marrow smears if they had failed to respond or VL relapsed after a full course of Sbv treatment. Pregnant or

lactating women, HIV-positive patients, and intravenous drug abusers were excluded from the trial. Patients were randomized into preassigned treatment groups by the sealed-envelope technique, and liposomal amphotericin B was administered by an independent coinvestigator who broke the seal of the envelope and prepared infusions. The drug was dissolved in 50–100 mL of 5% dextrose solution and administered for 30–60 min. No premedication was used. Patients, principal investigators, and other workers were blinded to the dose used. Codes were broken after the end of the study, after the completion of 6 months of follow-up for all the patients. Clinical examination and laboratory investigations were performed before treatment, immediately after treatment (Day 5), and 2 weeks after the end of treatment (Day 19). Splenic or marrow smears for parasitological examination were performed before the start of treatment and 2 weeks after the end of therapy (Day 19).

1. Apparent cure.

Evaluation of apparent cure was performed 2 weeks after the end of treatment (Day 19), which was defined as resolution of fever, regression of splenomegaly, and absence of parasites in splenic or marrow smear. Once apparent cure had been established, patients were followed for 6 months. If symptoms recurred within this period, splenic or marrow smears were examined for relapse of disease, and patients with documented relapse were given highdose (25 mg/kg) liposomal amphotericin B as rescue treatment.

2. Definite cure.

After posttreatment apparent cure, patients were followed for at least 6 months for evaluation of definite cure. Patients were designated as definitely

cured if there was absence of signs and symptoms of VL after 6 months of follow-up.

TABLE 1
Clinical and laboratory values of the 3 groups of patients treated with amphotericin B†

Group (cumulative dose)	Group A (3.75 mg/kg)		Group B (7.5 mg/kg)		Group C (15 mg/kg)	
	Pretreatment	Posttreatment	Pretreatment	Posttreatment	Pretreatment	Posttreatment
Age, year (range)	12 ± 1.74* (8–16)		24 ± 1.15 (18–23)		23 ± 3.0 (17–29)	
Male (%)	60		60		53	
Weight (kg)	25 ± 0.59**	27 ± 0.6	34 ± 0.5	34 ± 0.5	32 ± 0.6	33 ± 0.6
Spleen size (cm)	9.1 ± 0.9	2.9 ± 2.5	9.3 ± 0.9	2.6 ± 0.5	9.5 ± 0.9	3.1 ± 0.4
Hemoglobin (g/dL)	7.6 ± 0.4	9.8 ± 0.3	7.3 ± 0.3	9.9 ± 0.3	7.7 ± 0.4	9.7 ± 0.4
Platelets (×10 ⁹ /L)	154 ± 13	275 ± 19	165 ± 23	244 ± 19	142 ± 8	243 ± 13
Serum creatinine (µmol/L)	0.75 ± 0.05	0.66 ± 0.03	0.75 ± 0.04	0.77 ± 0.04	0.82 ± 0.05	0.80 ± 0.05
Alanine aminotransferase (IU/L)	24 ± 4	20 ± 1	31 ± 8	24 ± 2	24 ± 2	22 ± 2

* P = 0.002.

** P = 0.043.

† All values are expressed as mean ± standard error of mean. Pretreatment = day 0; posttreatment = Day 19.

3. Statistical analysis.

Comparison of the trial groups was performed by the Kruskal-Wallis test for ordinal/continuous data (and the chi-square test for nominal data). The Conchran Armitage trend test was used to evaluate dose response. Fisher’s exact test was used to compare groups by means of pairwise comparison with 95% confidence intervals. The Wilcoxon matched-pair signed-rank test was used to evaluate changes from baseline. The sample size calculation was based on a complete cure rate hypothesis of 90% for the highest dose and 50% for the lowest dose. To detect a difference of 40% in cure rates with a power of 80% and a significance level of 5% in a 2-tailed approach, 25 patients per treatment arm were required.

3. RESULT

Eighty-four patients were treated with this protocol, 28 patients in each of the 3 groups. Seventy-eight (93%) of 84 patients were unresponsive to their initial sodium stibogluconate treatment; the remaining 6 patients (7%) relapsed after initial cure. Clinical and laboratory characteristics of the patients are provided in Table 1. Although randomization and treatment was blinded, Group A was significantly younger, which contributed to the lower mean weight

(P 0.043) of this group. Otherwise no significant difference in other clinical or laboratory parameters between groups was seen. At posttreatment evaluation on Day 19, a decrease in spleen size and rise in hemoglobin, white blood cell count, and platelets were seen. Compared with baseline values, changes in these parameters were similar among the 3 groups and was not drug-dose dependent (Table 1). One patient each in Groups A and B had detectable parasites in splenic smears; these patients were considered to have failed to respond to primary treatment. One patient in Group C failed to return for the Day 19 follow-up. Thus, in the initial short-term, posttreatment evaluation, 27 patients (96%) each were free of parasites and were considered apparently cured. Patients were followed up for 180 days. Two patients in Group A, one in Group B, and one in Group C relapsed with recurrence of fever, splenic enlargement, and presence of parasites in the splenic/marrow smears. The missing patient of Group C returned for a final evaluation at Day 180 and was found to be free of disease. Nonresponding patients as well as those who relapsed during the follow-up period were given a high dose of amphotericin B (25 mg/kg cumulative dose) as rescue medication and were cured successfully. None of the patients died during the study.

TABLE 2
Response to amphotericin B therapy in Indian visceral leishmaniasis

Cumulative dose	3.75 mg/kg, n (%)	7.5 mg/kg, n (%)	15 mg/kg, n (%)
Total number of patients	28	28	28
Apparent cure (at Day 19)	27 (96)	27 (96)	27* (96)
Initial failure (at Day 19)	1 (4)	1 (4)	–
Relapse	2 (7)	1 (4)	1 (4)
Definite cure (at Day 180)	25 (89)	26 (93)	27 (96)

* One patient did not come back for apparent cure evaluation; however, at 6 months, he was available for final evaluation.

With a cumulative dose of 3.75 mg/kg (Group A), 7.5 mg/kg (Group B), and 15 mg/kg (Group C) of liposomal amphotericin B, long-term (definite) cure occurred in 89, 93, and 96% patients, respectively.

No significant difference was seen between the cure rates of the 3 groups (Table 2). Overall, liposomal amphotericin B was well tolerated. The most frequent side effects were observed during infusion. Forty-six episodes of infusion-related rigors were experienced by 37 patients (96%); 91% of the episodes were of mild intensity. Thirty patients (36%) experienced rigor only once. Similarly, 49 episodes of fever were recorded in 25 patients (30%), occurring only once in 13 of the 84 patients included in the trial. Elevation of temperature was considered mild in 34 of 49 of the episodes, and 11 episodes were of moderate intensity. Eight patients (30%) experienced back or lumbosacral pain, which in 2 patients was of severe intensity. This occurred in one patient each of Groups B and C. Seven patients (8%) had one episode of vomiting during the treatment period. There was no significant change in renal or hepatic biochemistry, although in 7 patients (8%), there was grade I rise (up to 1.26–2.5 times of upper limit of normal value) in serum creatinine, which had returned to normal by the posttreatment evaluation on Day 19. No hepatic or bone marrow toxicity was detected. Overall, the incidence of adverse reactions was similar among the 3 treatment groups. No serious adverse events related to this formulation of liposomal amphotericin B were recorded.

4. Discussion

The liposomal amphotericin B preparation was effective in curing antimony-unresponsive patients in all 3 dosage groups. In India, conventional amphotericin B has been shown to be remarkably effective at low doses in the treatment of VL. The lowest reported effective cumulative dose of conventional amphotericin B has been 7 mg/kg, with a cure rate of 98%.¹⁵ In one study, 84% of the patients, who were treated with a cumulative dose of

5 mg/kg of amphotericin B lipid complex (Abelcet, Liposome Co., Princeton, NJ), were cured of Indian VL.⁸ Liposomal amphotericin B is approved in several European countries for primary treatment of VL, and the U.S. Food and Drug Administration approved it recently, recommending a total dose of 21 mg/kg¹⁶; however, in a pilot trial in Indian VL, liposomal amphotericin B in cumulative doses of 6, 10, and 14 mg/kg cured all 10, 9, and 10 patients, respectively.¹¹ The cumulative dose of 3.75 mg/kg of amphotericin B is by far the lowest total dose of amphotericin B used for the treatment of VL. Nevertheless, even at this low dose, 96% of patients were cured initially, a rate similar to those treated with 7.5 and 15 mg/kg. Given that 2 patients in the 3.75 mg/kg group and one each in 7.5 and 15 mg/kg group relapsed, a definite cure rate of 89, 93, and 97% was achieved with these 3 groups, respectively. The differences in these cure rates were not statistically significant because the sample size was too small to measure a small effect. Although infusion-related reactions were measured, they were milder than those usually seen with conventional amphotericin B treatment. Although clinical availability of liposomal amphotericin B is a major therapeutic advance in the treatment of leishmaniasis, it may remain out of reach of most patients with VL because of its higher cost. The low-dose regimens evaluated here not only reduce the cost by one third to one sixth of the currently recommended doses, but the shortened duration of treatment reduces the usual hospital stay from 5 weeks or more to just 5 days. The shortened hospital stay will further reduce the hospital cost and the person-days lost for both patients and attendants, and it will increase the availability of hospital beds 6- to 7-fold. Although hospital and other associated costs in India are not high, they can partially offset the higher cost of the drug. The decreased number of infusions from 15 or more to 5 reduces the costs of fluids, tubing, and other hospital supplies. Of course,

patients who either fail to respond to treatment or who relapse after initial cure have to be retreated, and while calculating the cost of therapy, we took into account the cost of retreating this subset of patients. Safety of antileishmanial drugs is a major concern in the treatment of VL, as all available antileishmanial drugs result frequently in drug-induced toxicity. Conventional amphotericin B is frequently associated with moderate to severe infusion-related reactions. Premedications such as antipyretics, antihistamines, and hydrocortisone are often used. Thrombophlebitis and sudden death due to drug-induced myocarditis are other serious problems encountered with conventional amphotericin B.^{5,6} In this trial, the incidence of adverse reactions was low, and they were minor. In some patients, a mild but reversible rise in serum creatinine was observed. Infusion-induced reactions of a milder nature were only seen in one third of the patients, and these did not require any intervention. Infusion-related side effects with amphotericin B occurred less frequently compared with amphotericin B lipid complex.⁷ This trial supports other reports in the conclusion that that liposomal amphotericin B can be used at low doses in a short course without compromising its efficacy.¹⁷ Although no statistically significant differences were measured between the 3 treatment groups, the lowest effective cumulative dose reaching the definite cure rate level of 90% is 7.5 mg/kg. Liposomal amphotericin B is safe and well tolerated. However, if it is to be used in epidemics in Bihar or elsewhere in the world on a large scale, purchase of this drug needs to be available commensurate with resources of the health care system.

[REFERENCES]

1. Bora D, 1999. Epidemiology of visceral leishmaniasis in India. *Natl Med J India* 12: 62–68.
2. Sundar S, Singh VP, Sharma S, Makharia MK, Murray HW, 1997. Response to interferon- plus pentavalent antimony in Indian visceral leishmaniasis. *J Infect Dis* 176: 1117–1119.
3. Thakur CP, Sinha GP, Pandey AK, Kumar N, Kumar P, Hasan SM, Narain S, Roy RK, 1998. Do the diminishing efficacy and increasing toxicity of sodium stibogluconate in the treatment of visceral leishmaniasis in Bihar, India, justify its continued use as a first-line drug? An observational study of 80 cases. *Ann Trop Med Parasitol* 92: 561–569.
4. Jha SN, Singh NKP, Jha TK, 1991. Changing response to diamidine compounds in cases of kala-azar unresponsive to antimonial. *J Assoc Physicians India* 39: 314–316.
5. Thakur CP, Sinha GP, Pandey AK, Ahmed S, 1995. Cure of 72 antimony and pentamidine resistant kalaazar cases with amphotericin B. *Bihar J Internal Med* 1: 25–30.
6. Jha TK, Giri YN, Singh TK, Jha S, 1995. Use of amphotericin B in drug-resistant cases of visceral leishmaniasis in north Bihar. *Am J Trop Med Hyg* 52: 536–538.
7. Sundar S, Murray HW, 1996. Cure of antimony-unresponsive Indian visceral leishmaniasis with amphotericin B lipid complex. *J Infect Dis* 173: 762–765.
8. Sundar S, Agrawal NK, Sinha PR, Horwith G, Murray HW, 1997. Short-course, low dose amphotericin B lipid complex therapy for visceral leishmaniasis unresponsive to antimony. *Ann Intern Med* 127: 133–137.
9. Sundar S, Goyal AK, Mandal AK, Makharia MK, Singh VP, Murray HW, 1998. Amphotericin B lipid complex in the management of antimony

unresponsive Indian visceral leishmaniasis. *J Assoc Physicians India* 47: 186–188. 146 SUNDAR AND OTHERS

10. Sundar S, Goyal AK, More DK, Singh MD, Murray HW, 1998. Treatment of antimony-unresponsive Indian visceral leishmaniasis with ultra-short courses of amphotericin B lipid complex. *Ann Trop Med Parasitol* 92: 755–764.

11. Thakur CP, Pandey AK, Sinha GP, Roy S, Behbehani K, Olliaro P, 1996. Comparison of three treatment regimens with liposomal amphotericin B (AmBisome) for visceral leishmaniasis in India: a randomized dose-finding study. *Trans R Soc Trop Med Hyg* 90: 319–322.

12. Dietze R, Milan EP, Berman JD, Grogl M, Falqueto A, Feitosa TF, Luz KG, Suassuna FA, Marinho LA, Ksionski G, 1993. Treatment of Brazilian kala-azar with a short course of Amphocil (amphotericin B cholesterol dispersion). *Clin Infect Dis* 17: 981–986.

13. Davidson RN, Martino LD, Gradoni L, Giacchino R, Russo R, Gaeta GB, Pempinello R, Scott S, Rainondi F, Cascio A, Prestileo T, Caldeira L, Wilkinson RJ, Bryceson ADM, 1994. Liposomal amphotericin B (AmBisome) in Mediterranean visceral leishmaniasis: a multi-centre trial. *Q J Med* 87: 75–81.

14. Seaman J, Boer C, Wilkinson R, de Jong J, de Wilde E, Sondorp E, Davidson R, 1995. Liposomal amphotericin B (AmBisome) in the treatment of complicated kala-azar under field conditions. *Clin Infect Dis* 21: 188–193.

15. Mishra M, Biswas UK, Jha DN, Khan AB, 1992. Amphotericin versus pentamidine in antimony-unresponsive kala-azar. *Lancet* 340: 1256–1257.

16. Meyerhoff A, 1999. U.S. Food and Drug Administration approval of AmBisome (liposomal amphotericin B) for treatment of visceral leishmaniasis. *Clin Infect Dis* 28: 42–48.

17. Berman JD, Badaro R, Thakur CP, Wasunna KM, Behbehani K, Davidson R, Kuzoe F, Pang L, Weerasuriya K, Bryceson AD, 1998. Efficacy and safety of liposomal amphotericin B (AmBisome) for visceral leishmaniasis in endemic developing countries. *Bull World Health Organ* 76: 25–32

Author Guidelines

Publishing your research content in ScholarGen Publishers. To help you to easily publish your manuscript and to ensure that you are aware of all the procedures of publishing, you are requested to go through our guidelines and detailed illustrations. Following illustrations will help you to understand the steps involved in publishing your manuscript in ScholarGen Publishers.

Select a Journal

How to select the journals?

The journal you wish to publish your article or manuscript should be on the similar subject line as that of your article. For example, “ScholarGen Publishers ” will accept articles on Life Science.

Prepare your Manuscript

You need to follow few guidelines to ensure that your article is well written and well received by the scientific community and researchers.

Plagiarism

According to the Merriam-Webster online dictionary, to “plagiarize” means:

- to steal and pass off (the ideas or words of another) as one’s own
- to use (another’s production) without crediting the source
- to commit literary theft
- to present as new and original an idea or product derived from an existing source

In other words, plagiarism is an act of fraud. It involves both stealing someone else’s work and lying about it afterward. Plagiarism is defined on delinquency in research as the stealing of another person’s ideas, tables, content, processes, results or words without citing the appropriate credit to be considered as crime. When it comes to plagiarism, content from the internet is equally comparable to information from appearing in a book or journal. ScholarGen Publishers does not encourage any form of plagiarism, thus we strongly recommend you to check your article content before you submit manuscript to any of our journals. Plagiarism can be checked through online plagiarism software tools (although they are not completely reliable) to minimize further complications.

Formatting Prerequisites

1. Cover Letter

Cover letter must include the list of authors, and title of the manuscript. Mention the name of ScholarGen Publishers and choice of interest to which the submission is sent. Cover letter should briefly communicate upon your study to previously published work. It should declare that the work is not published elsewhere. The article type should be mentioned (Research/ Review/ Short Communication/ Editorial/ Case Report/ Perspectives). Lists any suggested reviewers if any. Also, include current telephone and fax numbers, as well as postal and e-mail address of corresponding author to maintain communication.

Sample Cover Letter can be downloaded here: [Cover Letter](#)

2. File Types

Authors may submit their manuscript files in either of the mentioned formats like Word (as .doc or .docx). All the figures must be in either of gif/ tiff/ jpeg formats. The figure should be of high resolution and the figure legend word limit is 300 words.

If your manuscript is or will be in .doc format and contains equations, you must be following the instructions below to make sure that your equations are editable when the file enters production. We recommend you to use Math Type to create the equation.

3. Manuscript Organization

The following order remains same for all the article types except Abstract, Keywords remain mandatory for Research and Review. Word limits for Research/ Review/ Cases/ remain 5000 words where as for Short Communications/ Perspectives/ Editorials remain 1500 words. References cited are excluded in the word limit.

Order of Manuscript

- Title
- Abstract
- Keywords
- Abbreviations
- Introduction
- Materials and Methods (Research)
- Subheadings (Review and rest of the article types)
- Results and Discussion (Results for Research/ Discussion for rest of the article types)
- Conclusion
- Acknowledgements
- References

Title: The word limit of the title should not exceed 15 words. Title should be a proper description and relevant to the work provided. Font has to be set to Times New Roman Bold, Title case.

Abstract: Abstract should describe the main objectives of the study. It should be able to list out all the work briefly. Significance and the results of the study need to be precise briefly. Abstract ‘word limit’ should be limited to 300 words.

Note: Abstracts should be free of citations.

Keywords: The major keywords used in the study need to be mentioned. Keywords limit is not more than 7-10 words.

Abbreviations: If any abbreviations are used in the study, their first usage has to be mentioned in full form along with the usage abbreviation in brackets. If there are too many abbreviations they have to be mentioned below the keywords.

Introduction: Introduction should be able to provide the background of the study. It should also provide comprehensive insight on the purpose of the study and its significance. Introduction needs to be descriptive and citations need to be provided.

Materials and Methods: Particular details and/or practices for new approaches have to be mentioned. For the used protocols the proper citations has to be mentioned. Results have to be unique and not copied from any other sources. This section should present enough detail to permit researchers to fully replicate your study. We recommend authors to put forward detailed protocols for less well-established methods.

Results and Discussions: This section might be further divided in subdivisions. Results and discussions must be providing the results. Illustrate the results of the experiments, the interpretation of these results, and the conclusions.

Conclusion: Authors should elucidate how the results communicate to the theory presented as the basis of the study and provide a concise explanation of the allegation of the findings.

Acknowledgements: Authors need to provide the funding details and the grant numbers if any. They might acknowledge their supported work.

References: Authors need to provide the references used in the text. All the references should be clearly mentioned along with the names, years, title of the article, volume number and page number.

Submit Manuscript

Completed manuscript can be submitted at Submit Manuscript tab for the chosen Journal page.

Peer Review of Manuscript

Peer review is scrutinizing process where an article or a manuscript is scrutinized by members who are specialized in their field. Every article is subjected to peer review before it is published in ScholarGen Publishers Journals except Editorials.

Scholargen Journal of Medical Imaging

Volume 04 Number 01 December 2021

Copy right Scholargen Journal of Medical Imaging, All right reserved.

This is identical to the Creative Commons Attribution Non-Commercial Licence.

Published on December 30, 2021

Subscription info : office@scholargen.com

Open access on <https://scholargen.com/journals/journal-of-medical-imaging/>

 ScholarGen Publishers

